SANDIA REPORT

SAND95-8257 • UC-1409
Unlimited Release
Printed September 1995

Coal Combustion Science Quarterly Progress Report July - September 1994

Principal Investigators: Larry L. Baxter
Kevin A. Davis
Robert H. Hurt
Nancy Y.C. Yang

Edited by Donald R. Hardesty

Prepared by
Sandia National Laboratories
Albuquerque, New Mexico 87185 and Livermore, California 94551
for the United States Department of Energy
under Contract DE-AC04-94AL85000

Approved for public release; distribution is unlimited.

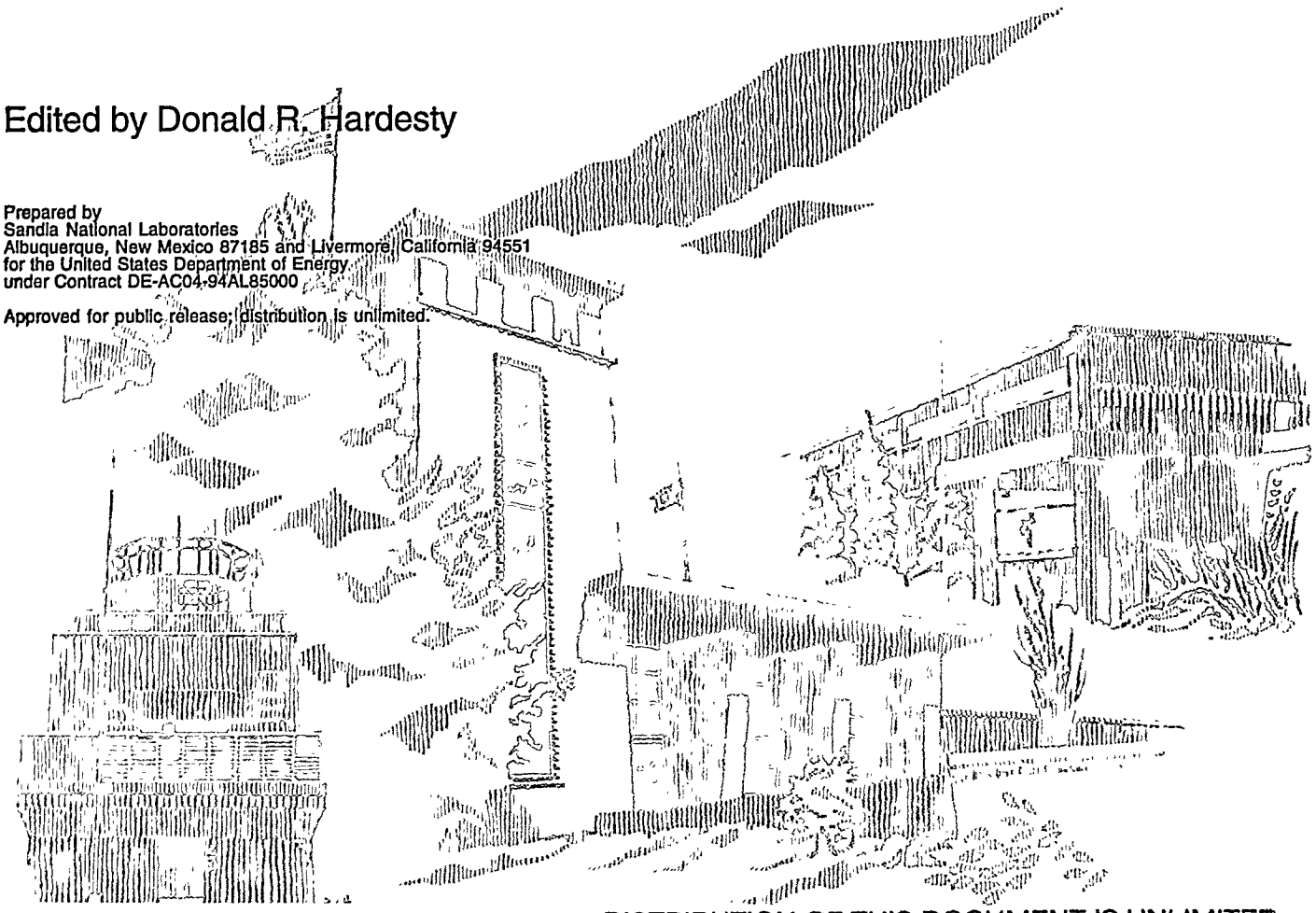

Issued by Sandia National Laboratories, operated for the United States Department of Energy by Sandia Corporation.

UC-1409

SAND 95-8257

Unlimited Release
Printed September 1995

COAL COMBUSTION SCIENCE

QUARTERLY PROGRESS REPORT

JULY - SEPTEMBER 1994

Submitted By: Donald R. Hardesty
Sandia National Laboratories, Livermore
Combustion Research Facility

Submitted To: Philip Goldberg
Pittsburgh Energy Technology Center

Research supported by the United States Department of Energy,
Office of Fossil Energy, Pittsburgh Energy Technology Center

COAL COMBUSTION SCIENCE

QUARTERLY PROGRESS REPORT — JULY - SEPTEMBER 1994

Donald R. Hardesty
Combustion Research Facility
Sandia National Laboratories
Livermore, California 94551-0969

This document is a quarterly status report of the Coal Combustion Science Project that is being conducted at the Combustion Research Facility, Sandia National Laboratories, Livermore, California. The information reported is for the period July - September 1994.

The objective of this work is to support the Office of Fossil Energy in executing research on coal combustion science. This project consists of basic research on coal combustion that supports both the Pittsburgh Energy Technology Center (PETC) Direct Utilization Advanced Research and Technology Development Program, and the International Energy Agency (IEA) Coal Combustion Science Project.

Specific tasks include:

Task 1: Kinetics and Mechanisms of Pulverized Coal Char Combustion

The objective of this task is to characterize the combustion behavior of selected U.S. coals under conditions relevant to industrial pulverized coal-fired furnaces. Work is being done in four areas: (a) kinetics of heterogeneous fuel particle populations; (b) char combustion kinetics at high carbon conversion; (c) the role of particle structure and the char formation process in combustion and; (d) unification of the Sandia char combustion data base. This data base on the high temperature reactivities of chars from strategic U.S. coals will permit identification of important fuel-specific trends and development of predictive capabilities for advanced coal combustion systems.

The principal investigator on this task is Robert H. Hurt.

Task 2: Deposit Growth and Property Development in Coal-Fired Furnaces

The objectives of this task are to provide a self-consistent database of simultaneously measured, time-resolved, ash deposit properties in well-controlled and well-defined environments and to provide analytical expressions that relate deposit composition and structure to deposit properties of immediate relevance to PETC's Combustion 2000 program. The task includes the development and use of diagnostics to monitor, *in situ* and in real time, deposit properties, including information on both the structure and composition of the deposits.

The principal investigator on this task is Larry L. Baxter.

TABLE OF CONTENTS

COAL COMBUSTION SCIENCE

QUARTERLY PROGRESS REPORT
JULY — SEPTEMBER 1994

EXECUTIVE SUMMARY

Task 1: The Kinetics and Mechanisms of Pulverized Coal Char Combustion

Work this quarter aimed at further defining the kinetics of char combustion to high carbon conversion and further unifying the Sandia char combustion data base. Two techniques that have proven very useful for the investigation of carbon burnout phenomena are captive particle imaging (CPI) and high resolution transmission electron microscopy (HRTEM) fringe imaging. Our previous quarterly reports have demonstrated the use of these techniques and have applied them to a limited number of coal or char samples. Work this quarter extends the application of these two techniques to other coals with emphasis on understanding rank effects in carbon burnout.

This quarter dual camera CPI experiments were performed on a set of four coals of varying rank to determine the effect of rank on both early and late stage combustion behavior. These coals are PSOC-1508D, Pocahontas #3 low volatile bituminous coal; PSOC-1493D, Illinois #6 high volatile bituminous coal, PSOC-1488D, Dietz subbituminous coal; and PSOC-1507D, Beulah lignite. This technique has also been applied to Pittsburgh #8 coal, and to three biomass-derived chars derived from pine, oak, and switchgrass (under other sponsorship). In all, captive particle image sequences have now been recorded for three U.S. bituminous coals, one subbituminous coal, one lignite, and three biomass-derived chars. The qualitative and quantitative behavior as a function of rank is described in this report.

In addition, during the quarter, high resolution transmission electron microscopy (HRTEM) fringe images were obtained and analyzed for a series of partially combusted chars from the high rank Pocahontas #3 coal (PSOC-1507D) to examine the effect of rank on the dynamics of char carbon crystalline rearrangements.

Task 2: Deposit Growth and Property Development in Coal-Fired Furnaces

During this quarter, emission FTIR analyses of ash deposit samples from PSI Technology company were initiated to evaluate the extent to which we can determine the transitions from Fe^{2+}- to Fe^{3+}-based silicates during oxidation. During the quarter, we demonstrated an ability to distinguish the silicates generally and are completing the investigation to determine if we can distinguish them from the types of deposits generated at PSI. Initial scans of the two samples are completed and analysis is underway. Higher resolution scans are being completed. Tunable diode laser characterizations are also progressing. Three new diode lasers were acquired and installed. They are under evaluation for tunability and region in which they lase. A combination liquid-

helium-cooled dewar detector and lock-in amplifier was brought on line and is being used to analyze the beam.

Also during the quarter, work continued to develop the theory being used to describe spectral emissivities of particulate layers. Computer coding of the mathematics was partially completed and debugged. In this report this theory is described in some detail. The theory is based on a combination of a first-principles generalization of Mie theory and a solution to the radiative transport equation. Example calculations from the portion of the theory that has been coded have been verified by comparing them with known solutions to the Mie scattering problems published by others.

In addition, work continued on our investigation of the high-temperature corrosion of ceramics. This is being done in collaboration with Combustion 2000 contractors. The emission FTIR diagnostic is being used to verify additional mechanisms not currently discussed for the corrosion of the material in alkali environments. The additional mechanisms, if found to proceed at rates comparable to the condensed sulfate-salt corrosion mechanism currently proposed, will significantly shorten the lives of SiC components at high temperatures compared to the current projections.

Future Work

On the char combustion task, during the next quarter, analysis of the CPI and HRTEM data will continue. In addition, work on the conversion-dependent submodel for char oxidation will be completed. Finally, we expect to complete the carbon burnout model, for use in the overall Sandia char oxidation model.

On the ash deposition task, during the next quarter, the new tunable diode lasers will be characterized and a sample cell will be used to verify their application to alkali vapors in a clean environment. The proper lasers will be selected for further use on the project. Also, the first phase of the emission FTIR spectroscopy analyses of iron-containing glasses will be completed. Finally, the theoretical description of the emissivity of particulate layers will also be completed.

PROJECT TITLE: **COAL COMBUSTION SCIENCE**

TASK 1: KINETICS AND MECHANISMS OF PULVERIZED COAL CHAR COMBUSTION

ORGANIZATION: **Sandia National Laboratories, Livermore**

CONTRACT: **FWP 0709**

REPORTING PERIOD: **July 1 - September 30, 1994**

REPORTED BY: **R. H. Hurt, K. A. Davis, N.Y.C. Yang, and D. R. Hardesty**

Phone: (510) 294-3707 and (510) 294-2321

OBJECTIVE FOR TASK 1

The objective of Task 1 is to characterize the combustion behavior of selected U.S. coals under conditions relevant to industrial pulverized coal-fired furnaces. In Sandia's Coal Combustion Laboratory (CCL), optical techniques are used to obtain high-resolution images of individual burning coal char particles and to measure, *in situ*, their temperatures, sizes, and velocities. Detailed models of combustion transport processes are then used to determine kinetic parameters describing the combustion behavior as a function of coal type and combustion environment. Partially reacted char particles are also sampled and characterized with advanced materials diagnostics to understand the critical physical and chemical transformations that influence reaction rates and burnout times. The ultimate goal of the task is the establishment of a data base of the high temperature reactivities of chars from strategic U.S. coals, from which important trends may be identified and predictive capabilities developed.

Research is divided into the four subtasks described below, in accordance with the FY92 - FY94 project plan.

Subtask 1.1 Kinetics of Heterogeneous Fuel Particle Populations

The objective of this subtask is to develop quantitative descriptions of single-particle combustion behavior and to identify their implications for global rates and for the performance of combustion systems. Experiments in the CCL provide a wealth of unique information on the combustion behavior of single particles as distinguished from macroscopic samples. Kinetic expressions based on population statistics are being developed that more accurately describe the char combustion process as it proceeds into the important region of high carbon conversion. One-dimensional combustion models are being applied to char particle populations, exhibiting realistic heterogeneity in size and reactivity, to identify the important mechanisms leading to unburned carbon in fly ash.

Subtask 1.2 Char Combustion Kinetics to High Carbon Conversion

The amount of unburned carbon in fly ash is an important concern in the design and operation of pulverized coal fired boilers. High carbon content represents a loss of efficiency, and prevents the sale of the fly ash byproduct as a raw material for the cement or construction industries. The objective of this subtask is to determine char oxidation kinetics valid to high carbon conversion (> 99%) and to identify and understand the mechanisms determining unburned carbon levels in fly ash from pulverized coal combustion. Fly ash samples are generated under carefully controlled laboratory conditions, and the mode of occurrence and properties of the residual carbon will be characterized. The high-temperature combustion reactivity of the residual carbon is measured and carbon transformations occurring during the combustion process are characterized. The ultimate goal of the subtask is the development and validation of an advanced char oxidation model for accurate prediction of residual carbon levels.

Subtask 1.3 The Role of Particle Structure and the Char Formation Process in Combustion

In pulverized coal combustion the process of devolatilization determines, to a large extent, the properties and thus the reactivity of the resulting char. Swelling coals, in particular, produce a variety of char particle morphologies ranging from dense consolidated particles to thin or thick walled cenospheres, depending in part on devolatilization conditions. The objective of this subtask is to generalize the kinetic results obtained in the CCL to other devolatilization and combustion environments, through an improved understanding of the char formation process and its relationship to char combustion rates and burnout times. This is being achieved through a combination of flow reactor experiments and high-resolution single-particle imaging.

Subtask 1.4 Unification of Sandia Char Combustion Data Base

The objective of this subtask is to complete the documentation of the existing Sandia data base, and to develop therefrom correlations and models allowing prediction of char reactivity and properties under technologically relevant conditions as a function of temperature, oxygen pressure, and coal rank and type. An additional objective is a unified treatment of nitrogen release kinetics during coal combustion.

SUMMARY OF TECHNICAL PROGRESS DURING THIS QUARTER

Two techniques that have proven very useful for the investigation of carbon burnout phenomena are captive particle imaging (CPI) and high resolution transmission electron microscopy (HRTEM) fringe imaging. Previous reports have demonstrated the use of the two techniques and have applied them to a limited number of coal or char samples. Work this quarter extends the application of these two techniques to other coals with emphasis on understanding rank effects in carbon burnout. This work falls within Subtasks 1.2 and 1.4, described above. The results and discussion are presented below in two sections, the first dealing with CPI experiments and the second with HRTEM analyses.

Captive Particle Imaging Experiments on Coals of Various Rank

The captive particle imaging experiment has been described in detail elsewhere [Hurt and Davis, 1994; Hurt et al., 1993, 1994a]. Dual camera experiments were performed this quarter on a set of four coals of varying rank to determine the effect of rank on both early and late stage combustion behavior. These coals are PSOC-1508D, Pocahontas #3 low volatile bituminous coal; PSOC-1493D, Illinois #6 high volatile bituminous coal, PSOC-1488D, Dietz subbituminous coal; and PSOC-1507D, Beulah lignite. This technique has also been applied to Pittsburgh #8 coal [Hurt and Davis, 1994], and three biomass-derived chars† derived from pine, oak, and switchgrass [Davis, 1994]. In all, captive particle image sequences have now been recorded for three U.S. bituminous coals, one subbituminous coal, one lignite, and three biomass-derived chars. The qualitative and quantitative behavior as a function of rank is described in the sections below.

Qualitative Observations

Swelling behavior

Because raw coals were used (rather than preprepared chars) these experiments revealed information on softening and swelling behavior prior to the onset of char oxidation. Softening and swelling was observed for most of the bituminous coal particles, although the extent of swelling varied greatly from particle to particle. Some particles are observed to solidify and stabilize at their maximum diameters, while other particles exhibit a rapid partial contraction prior to the onset of char oxidation. In some cases, the thermal contraction is not clearly distinguishable from size reduction due to oxidation in the early phases of char combustion. The majority of lignite particles and subbituminous particles showed no softening or swelling, although a very small number of the particles swell as much as a typical bituminous coal particle. Statistics on single particle swelling factors were presented in the previous quarterly [Hurt et al., 1994b].

Reactivities

All of the coals were initially investigated under a common set of combustion conditions (6 vol-% oxygen, 1250 K gas temperature). Judging by peak particle temperatures and burnout times, the relative reactivity of these chars is:

Beulah > Illinois #6 > Pittsburgh #8 > Pocahontas #3

Reactivities thus fall in strict rank order as:

lignite > high vol. C bit. > high vol. A bit. > low vol. bit.

which has also been observed for this same set of coals in entrained flow reactor experiments at gas temperatures of 1500 - 1650 K [Hurt and Mitchell, 1994].

---

† Work funded by the Department of Energy through the National Renewable Energy Laboratory.

Extinction and final burnout

In these early CPI experiments, it was apparent that the low and high rank materials behave very differently during the late stages of combustion. The three bituminous coals exhibit an early near-extinction followed by a slow final burnout, as has been discussed previously [Hurt and Davis, 1994]. The low-rank coals particles, in contrast, maintain high combustion temperatures throughout more of the burnout process, extinguishing at or near the point of complete carbon consumption. In some cases, a shrinking core burning carbon is observed within a cloak of translucent ash, and that core remains highly incandescent until it disappears, leaving an apparently carbon-free ash particle†. The biomass chars have also been observed to undergo a similar late extinction behavior [Davis , 1994].

The initial experimental conditions were not, however, perfectly suited for quantitative investigation of extinction phenomenon. Under these conditions, the lignite burned so quickly that much of the reaction occurred during transient heating, while the highest rank coal (Pocahontas) burned too slowly to raise the particle temperature significantly above the inert particle limit. For quantitative comparison of complete burnout profiles, combustion conditions were tailored to match the char under investigation. These quantitative experiments are described below.

Quantitative Burnout Profiles

Captive particle imaging experiments were performed with the oxygen concentration, and to a lesser extent the gas temperature, adjusted for each coal to give comparable particle temperatures and thus comparable burning rates. Experiments on low rank coals were performed in 3 mol-% oxygen at a gas temperature of 1175 K. The high volatile bituminous coal experiments were performed in 6% oxygen at 1250 K and the low volatile coal experiments in 19% oxygen at 1250 K. Initial coal particle sizes were 125 - 210 μm. Image sequences were obtained for over one-hundred particles and recorded on tape.

Figures 1.1 and 1.2 present example burnout profiles in the form of time-resolved particle radiance measurements for three bituminous and four low-rank coal particles. This set of particles was selected from the much larger data set to illustrate typical behavior. Significant differences in peak temperature and burnout time are observed between individual particles from the same coal, as observed previously [Hurt et al., 1994b]. The high rank coals all show an early near extinction and a slow final burnout of the remaining carbon. Many of the Pocahontas coal particles exhibit a delayed ignition under these conditions, with the peak temperature occurring well after the initial transient heating period. Some ignition delay can be seen in the example profile presented in Fig. 1.1. As in the preliminary experiments, most low rank coal particles did not show the early near extinction.

---

† For ash particles that are opaque, it is not always possible to determine the point of complete carbon burnout. For particles with translucent ash, or with very small quantities of ash, complete carbon burnout is easily confirmed by the absence of material that is dark under reflected visible light. Significant numbers of particles of both types were observed in this study.

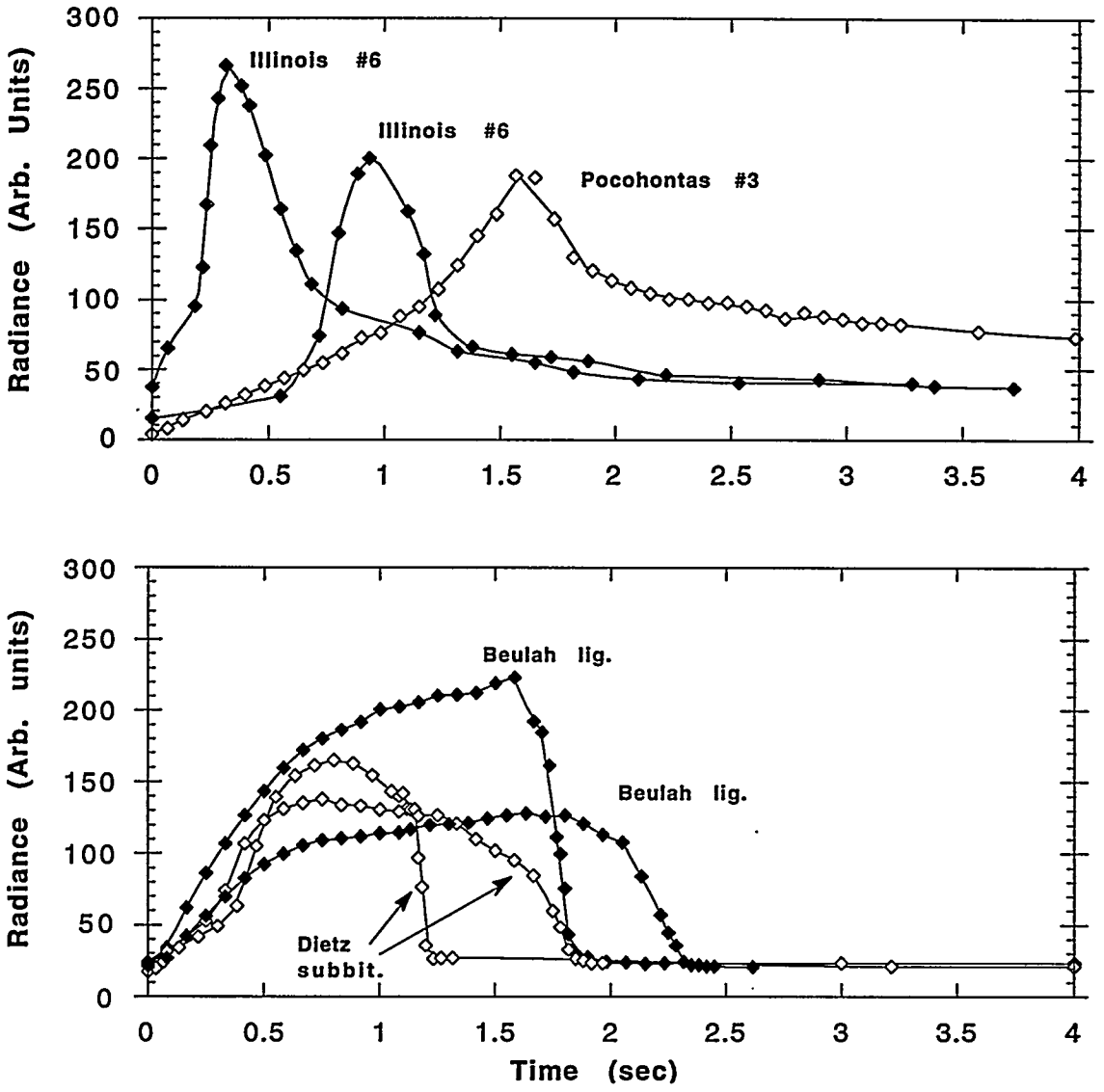

Figure 1.1 Single-particle burnout profiles for various coal chars determined by captive particle imaging. Initial coal particle size 125 - 210 μm. Combustion conditions: 3 mol-% oxygen at a gas temperature of 1175 K (for Beulah and Dietz coals); 6% oxygen at 1250 K (for the Illinois coal), and 19% oxygen at 1250 K (for the Pocahontas coal).

Figure 1.2 depicts the same data in normalized form to facilitate direct comparison of the shape of the burnout profiles. Normalized radiance is defined as L / L_{max} where L_{max} is the maximum radiance reached by the particle during its combustion lifetime. Normalized time is defined as t / t_{mns}, where t_{mns} is the time at which the profiles exhibit the maximum negative slope, a convenient definition of the point of near-extinction. This figure highlights the systematic

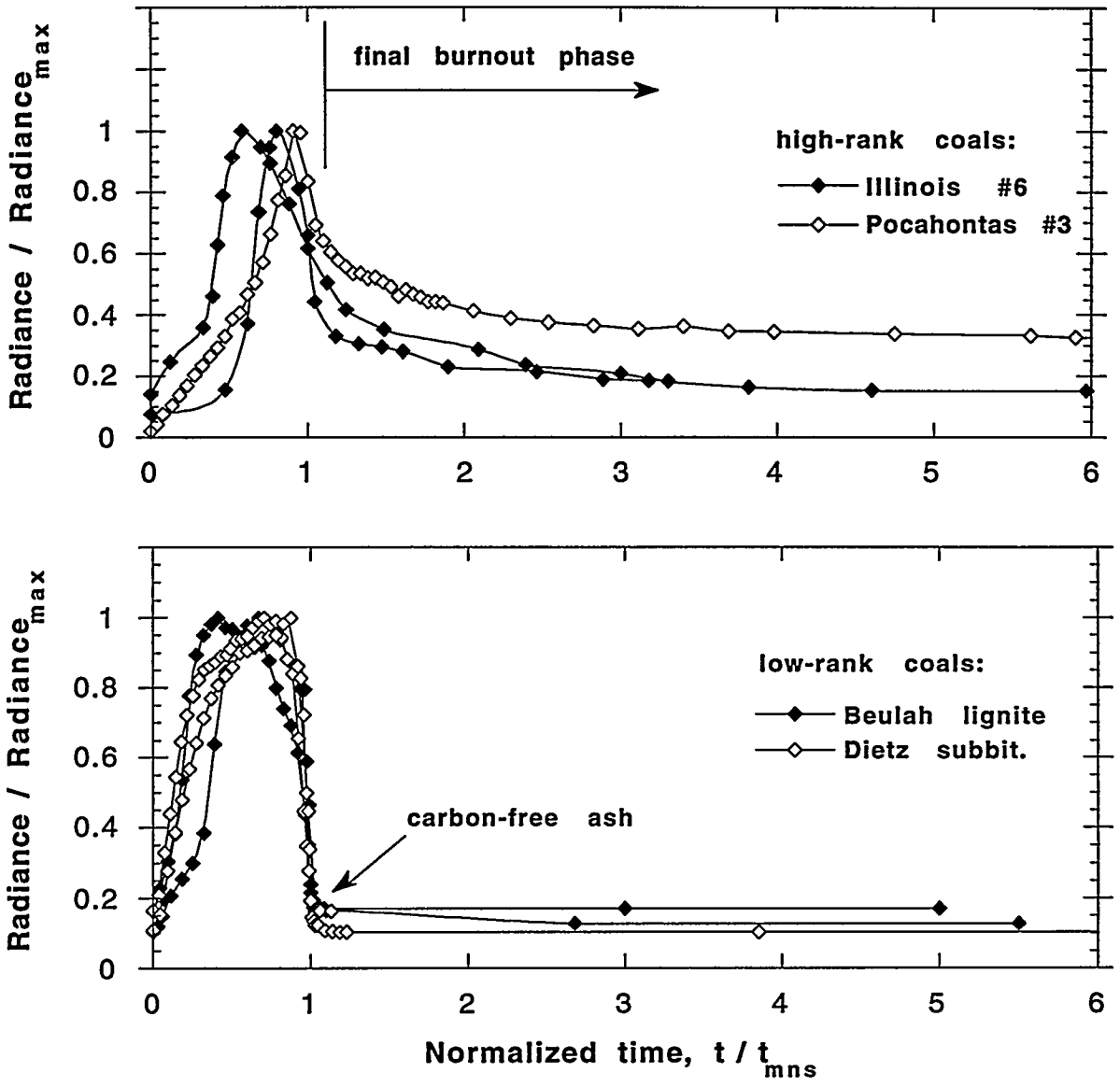

Figure 1.2 Normalized single-particle burnout profiles for various coal chars determined by captive particle imaging.

differences between the high and low rank coals. The normalized profiles for low rank coal particles show a common shape with an abrupt extinction event followed by a flat radiance profile. Typically, no carbon is observed after the extinction event. The high rank coals exhibit a similar maximum in particle radiance, but also a continued slow decrease in radiance following the abrupt near-extinction event. The slow decrease in radiance lasts from two to fifteen seconds and coincides with the slow conversion of a carbon-rich to an ash-rich particle as observed under reflected visible light through the second imaging channel. The initial abrupt decrease in radiance

is caused by an abrupt decrease in particle temperature; the slow decay thereafter is believed to be due to decreases in the spectral emissivity at roughly constant particle temperature.

Mechanisms

These experiments establish a systematic difference between the late stage combustion behavior of high and low rank coals, but do not establish the underlying mechanism that differentiates them. We can nevertheless speculate on the mechanism from our knowledge of carbon structure and coal properties. First, low rank materials have high oxygen contents that are partially retained in their chars. Oxygen is divalent and often found in functional groups that serve as crosslinks between aromatic units. Oxygen content thus inhibits the ultrafine structural rearrangements that lead to turbostratic carbon order and loss of reactivity. This has been directly observed in HRTEM studies of biomass char combustion [Wornat et al., 1994]. High oxygen content precursors are thermosetting and produce rigid char structures that remain disordered and reactive through the final stages of burnout.

Secondly, the presence of catalytic minerals in low-rank coals may affect the late stages of burning. Catalysis becomes less important with increasing temperature and is thought not to play a major role at peak particle temperatures in pulverized coal combustion. Catalysis may play a role, however, at the lower temperatures used in CPI studies or in the final burnout phase following char deactivation in entrained flow experiments. The presence of catalytic matter and its concentration in the latter stages of burnout may serve to maintain high char reactivity in the low rank coals.

Finally, inorganic impurities have also been shown to catalyze the oxidation of CO to CO_2 [Young and Niksa, 1987]. Approximately two-thirds of the heat of reaction in carbon oxidation is liberated in the CO oxidation step, so even modest amounts of CO_2 produced as a surface reaction product or from gas phase reactions within the pores of the particle can substantially elevate the particle temperature. Carbon dioxide production has been shown by Mitchell [1988] to be insignificant for particle temperatures above about 1800 K, but significant in some cases at lower temperatures. At 1250 K in CPI experiments, carbon dioxide production on or within the char particles could contribute to the high particle temperatures observed. Catalysis of this conversion by well-dispersed inorganic material in the low rank coals could lead to sustained high temperatures throughout burnout.

Implications for Boilers

These observations made under carefully controlled laboratory conditions help to explain the behavior of low rank coals in commercial combustion systems. Many low rank coals, especially lignites, burn to near completion in full-scale systems, leaving very little residual carbon in the fly ash. Such high conversions are not typically achieved for bituminous coals, including high volatile steam coals.

This difference between low rank coals and high volatile bituminous coals is not apparent in the early stages of the combustion process in a boiler. Using kinetic expressions derived from entrained flow reactor experiments [Mitchell et al, 1992; Hurt and Mitchell, 1992], one predicts

only slight differences in burning rates between the low rank coals and high volatile bituminous coals at 2000 K, representative of the temperature in the near-burner region in boilers. Only in the later stages of combustion do the differences between low rank coals and high-volatile bituminous coals become apparent. This report presents evidence that low rank coals are more resistant to deactivation and thus maintain a higher reactivity in the late stages of combustion. This is believed to be a key factor making high conversions possible during commercial combustion of low rank coals. Conversely, the tendency of bituminous coals to deactivate is a key factor limiting their ultimate burnout in industrial practice. The advanced char combustion model under development will account for these important differences in the late stages of burning and will help identify the detailed implications for boiler design and operation.

Crystalline Structure of Flame-Generated High Rank Coal Chars

In the past, we have used high resolution transmission electron microscope (HRTEM) fringe imaging to characterize the evolution of carbon crystalline structure during combustion of Illinois #6 char [Davis et al., 1994]. Identical measurements have also been made on biomass chars prepared from southern pine, a softwood; and switchgrass, an herbaceous material [Wornat et al., 1994]. An effort is currently underway to extend this work to coals of higher and lower rank. HRTEM analyses are being performed on partially combusted samples of Beulah lignite (PSOC-1507D), Pittsburgh #8 (PSOC-1451D), and Pocahontas #3 (PSOC-1508). This report presents the first results of this effort, a series of fringe images for four partially reacted samples of Pocahontas #3 char.

The char samples were prepared in the CCL entrained flow reactor by combustion in 20 mol-% oxygen at a nominal gas temperature of 1600 K. The oxygen content was chosen to produce particle temperature histories and degrees of conversion that are comparable to those experienced by the more reactive Illinois #6 coal in the earlier experiments. Samples were collected at residence times of 47, 72, 95, and 117 msec, corresponding to bulk char carbon conversions of 0, 27%, 42%, and 50%. The char samples were ground and placed on a holey carbon grid for HRTEM analysis at Sandia New Mexico.

Before presenting the results, let us consider how fringe images are obtained for highly anisotropic samples. Figure 1.3 shows an idealized graphitic flake with its layer planes oriented parallel to the substrate and exhibiting a curled edge or fracture surface. For such a sample, the lattice planes cannot be imaged with the focal plane parallel to the substrate — off the axis of preferred alignment, the image is featureless. Successful fringe imaging requires either inspection of the curled edge or specimen rotation by 90°. The same geometry applies to the Pocahontas #3 chars, which are not graphitic, but are highly anisotropic with the axis of preferred orientation perpendicular to the substrate.† The images shown here were acquired either by specimen tilting or by examination of a curled edge.

---

† This is a natural consequence of the grinding process, which produces fracture surfaces lying parallel to the layer planes. The resulting flake-like particles tend to lie on the substrate in the orientation shown in Fig. 1.3.

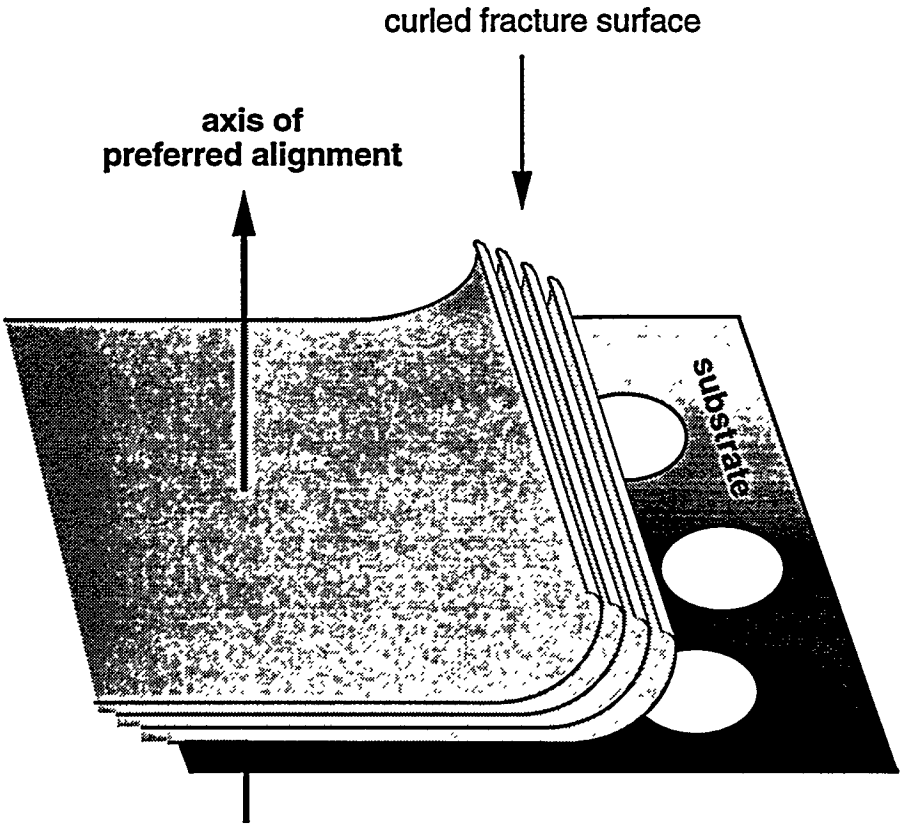

Figure 1.3 Ideal graphitic carbon flake with curled edge.

Figure 1.4 shows examples for the Pocahontas coal of HRTEM images taken both parallel to and off the axis of preferred orientation. All of char samples show a gross long-range anisotropy extending across the entire field-of-view (100 nm) in most images. Pocahontas #3 is a metallurgical coal, known for the development of optical texture (anisotropy) upon carbonization†. The present experiments show that long-range alignment can occur even for heating rates approaching 10^5 K/sec and heat treatment times of only 47 msec. The individual straight layer segments are limited in length, however, and the orientations are far from uniform. Off the axis of preferred alignment, the sample appears virtually amorphous with only a few stray layers or small crystallites visible (see Fig. 1.4).

Figure 1.5 shows on-axis HRTEM images for Pocahontas chars as a function of combustion residence time and char carbon conversion. Each image shows a well-developed turbostratic structure with a high degree of anisotropy. The Pocahontas coal does not undergo a transition from amorphous to turbostratic during char combustion, but rather has a fully turbostratic, highly

† During carbonization at slow heating rates, long-range anisotropy can develop in the fluid phase leading to distinct molecular orientation domains (MODs) which are incorporated in the char upon solidification. The MODs have optical properties that are directional and can be visualized directly with a polarizing microscope.

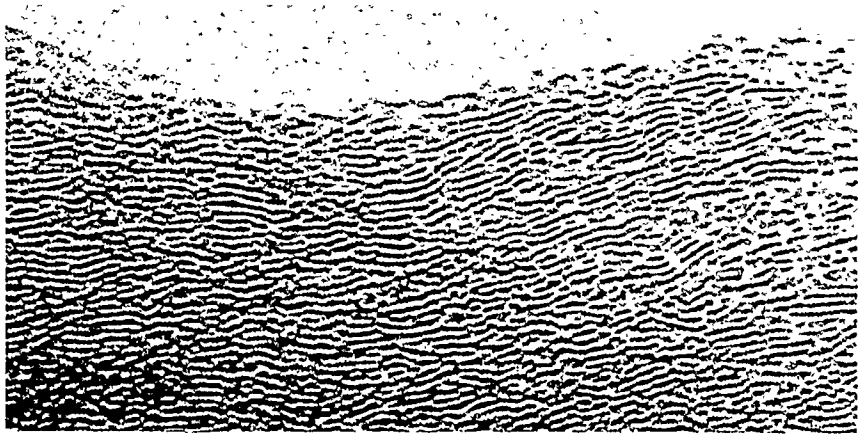

Image parallel to axis of preferred alignment

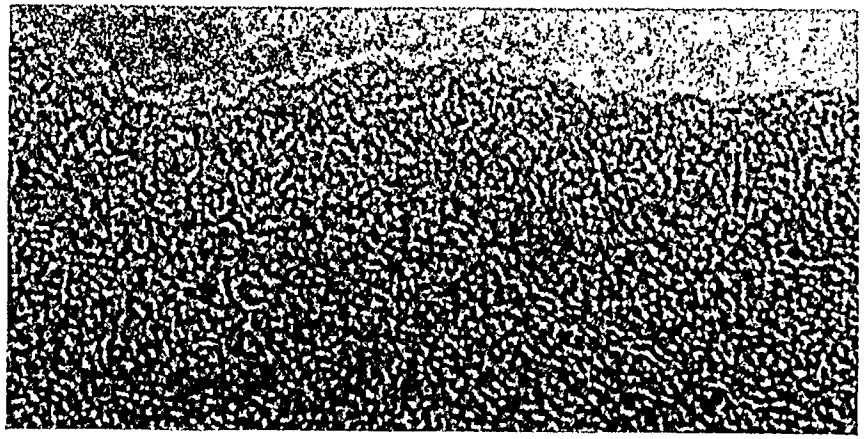

Off-axis image

Figure 1.4 HRTEM fringe images of Pocahontas #3 char after 47 msec residence time, at the onset of cha oxidation in the entrained flow reactor.

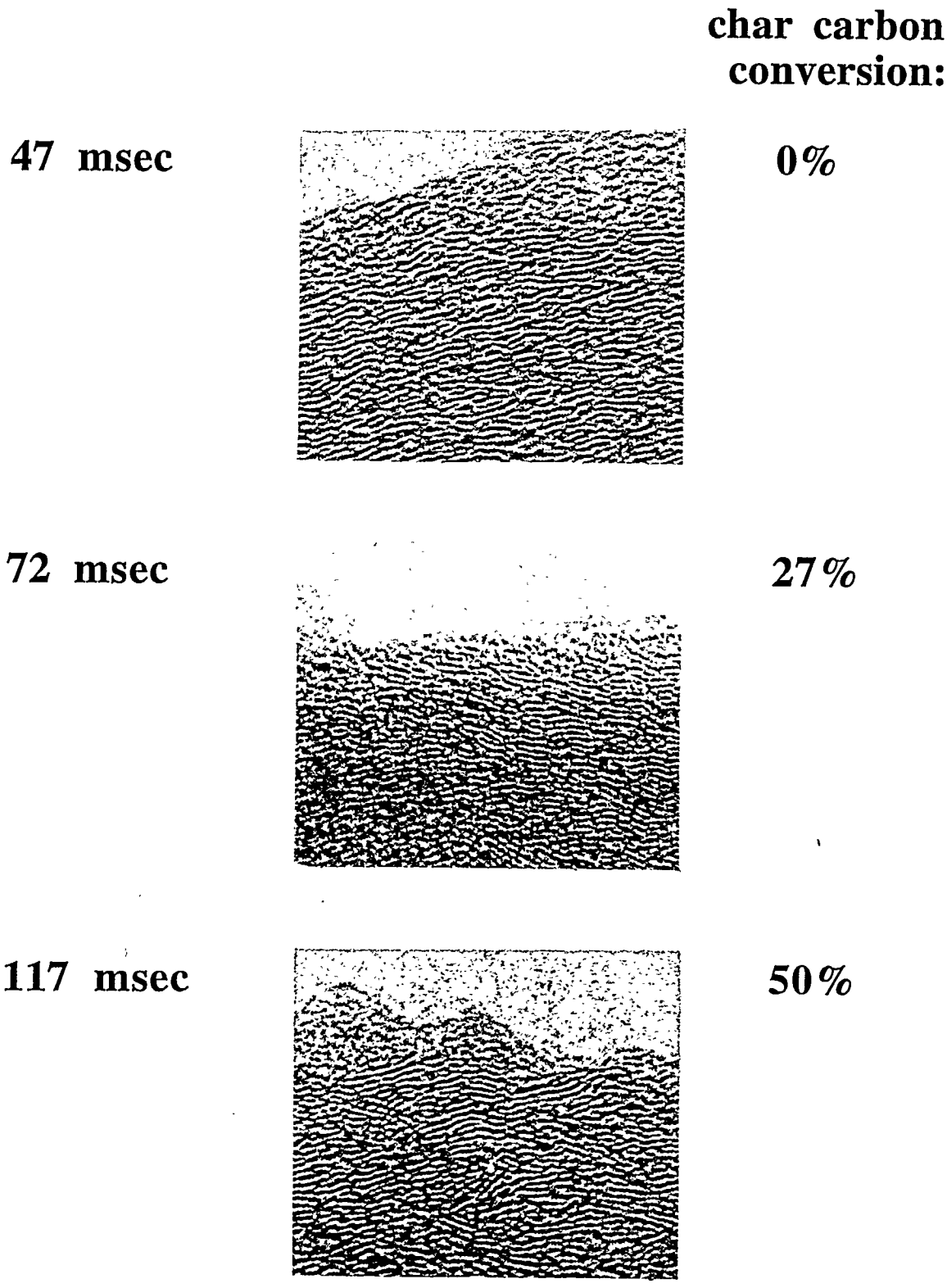

Figure 1.5 HRTEM fringe images of Pocahontas #3 chars after various stages of combustion in the entrained flow reactor. Focal plane is parallel to the axis of preferred orientation in all images.

anisotropic structure at the onset the char combustion phase. It is not yet clear whether the turbostratic order develops entirely during devolatilization, or whether long range order in the raw coal, perhaps associated with bedding plane anisotropy, influences char structure. An HRTEM analysis of the raw coal is therefore currently underway. For mid-rank coals such as Pittsburgh #8, it remains to be seen whether turbostratic order develops prior to char combustion (as the Pocahontas coal), or during char combustion (as the Illinois coal).

For Pocahontas coal, the heat treatment and oxidation that accompany char combustion may subtly improve the degree of order, but it is not obvious from the fringe images. Once the structure has become fully turbostratic, it is unlikely to be disrupted, and thus gross structural changes may not occur upon further heat treatment. Graphitization then proceeds through subtle improvements in the planarity of individual layers and the precise degree of parallelism between neighboring layers. Additional work is needed before this process can be quantitatively described using fringe imaging.

Finally, if we consider the complete set of chars investigated to date by HRTEM and rank them according to the degree of order observed in the fringe images (amount of turbostratic material) we obtain:

Biomass chars	~	Illinois #6 low conversion	>	Illinois #6 high conversion (117 msec)	>	Pocahontas #3 low conversion	~	Illinois #6 residual carbon	~	Daltex residual carbon

which precisely reproduces the ranking by combustion reactivity. The degree of order in fringe images may thus provide a useful correlation for the reactivity of chars from a variety of precursors and treatment conditions.

ACKNOWLEDGMENTS

Financial support for this work is provided by the U.S. DOE Pittsburgh Energy Technology Center's Direct Utilization Advanced Research and Technology Development Program. The technical contributions of James Ross of TAD technical services are gratefully acknowledged. Also acknowledged are the efforts and expertise of Thomas Headley at Sandia, New Mexico regarding HRTEM analyses.

NOMENCLATURE FOR TASK 1

L	spectral radiance in a band from 700 - 1000 nm.
L_{max}	maximum spectral radiance exhibited by a particle in its burning lifetime
t	time
t_{mns}	time at which the maximum negative slope (in L vs. t) occurs.

PUBLICATIONS, PAPERS, AND PRESENTATIONS

Papers and presentations on PETC-sponsored and related work were given at the 25th International Symposium on Combustion and at the EPRI Conference on the Effect of Coal Quality on Power Plants. The references are given below:

at the 25th Combustion Symposium:

Hurt, R. H. and Davis, K. A., "Near-Extinction and Final Burnout in Coal Combustion."

Davis, K. A., Hurt, R. H., Yang, N. Y. C., and Headley, T. H., "Evolution of Char Chemistry, Crystallinity, and Ultrafine Structure during Pulverized Coal Combustion."

Wornat, M. J., R. H. Hurt,, N . Y. C. Yang, and T. J. Headley, "Structural and Compositional Transformations in Biomass Chars during Combustion."

at the Coal Quality Conference:

Hurt, R.H., Davis, K. A., Yang, N.Y.C., and Gibbins, J. R. "Carbon Burnout in Pulverized Coal Combustion: An Overview of Mechanisms and Trends."

Man, C.K., Beeley, T.J., Gibbins, J.R., Lockwood, F.C., Williamson, J., Crelling, J.C., and Hurt, R.H. "Reactivity Measurements on Chars Formed at Combustion Temperatures—The Key to Burnout Prediction?"

In addition, a paper was accepted this quarter for publication in Fuel, entitled:

Hurt, R. H., Davis, K. A., Yang, N. Y. C., Headley, T. R., and Mitchell, G. "Residual Carbon from Pulverized Coal Fired Boilers 2: Morphology and Physicochemical Properties, accepted for publication in *Fuel*, 1994.

Finally, a presentation was given at the Tenth Annual Coal Preparation, Utilization, and Environmental Control Contractors Conference in Pittsburgh.

REFERENCES

Davis, K.A. "Combustion studies of pyrolysis oils and chars" D. R. Hardesty (Ed.), Sandia National Labs Quarterly Progress Report, August 15 - November 15, 1994.

Hurt, R. H. and Davis, K. A., "Near-Extinction and Final Burnout in Coal Combustion," accepted for publication in the *Proceedings of theTwenty-Fifth (International) Symposium on Combustion,* 1994

Hurt, R. H., Davis K. A. and Hardesty, D. R. in *Coal Combustion Science--Quarterly Progress Report,* Hardesty, D. R. (ed.), Sandia Technical Report, July - September (1993).

Hurt, R. H., Davis K. A. and Hardesty, D. R. in *Coal Combustion Science--Quarterly Progress Report,* Hardesty, D. R. (ed.), Sandia Technical Report, January - March (1994a).

Hurt, R. H., Davis K. A. and Hardesty, D. R. in *Coal Combustion Science--Quarterly Progress Report,* Hardesty, D. R. (ed.), Sandia Technical Report, April - June (1994b).

Hurt, R. H. and R. E. Mitchell. "Unified High-Temperature Char Combustion Kinetics for a Suite of Coals of Various Rank" *24th International Symposium on Combustion*, The Combustion Institute, Pittsburgh, PA, pp. 1243 - 1250 (1992)

Hurt, R. H., Mitchell, R. E., Baxter, L. L. and Hardesty, D. R. "Char Combustion Kinetics for U. S. Coals: A Comprehensive Data Base for Industry" Proceedings of the Ninth Annual International Pittsburgh Coal Conference, University of Pittsburgh, (1992)

Mitchell, R.E., *Twenty-Second Symp. (Int.) on Combustion*, The Combustion Institute, Pittsburgh, pp. 69-78, 1988.

Wornat, M. J., R. H. Hurt,, N . Y. C. Yang, and T. J. Headley, "Structural and Compositional Transformations in Biomass Chars during Combustion" accepted for publication in *Combustion and Flame*, 1994.

Young, B.C., and Niksa, S., "Combustion Rates for Selected Low-Rank Coal Chars," *1987 International Conference on Coal Science*, J.A. Moulijn et al., ed. Elsevier Science Publishers, Amsterdam, 1987.

Task 1
Six Month Plan and Milestone Chart

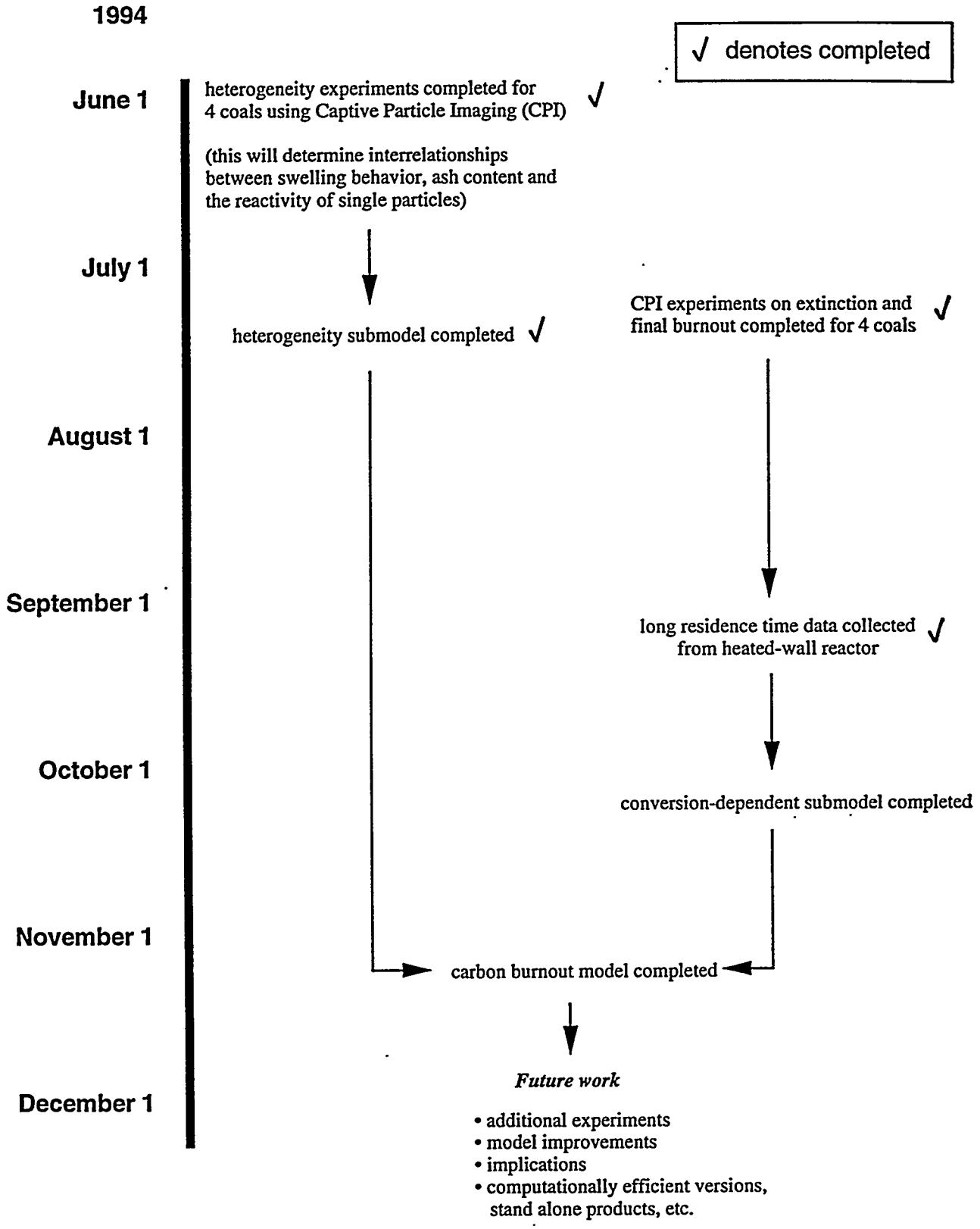

PROJECT TITLE:	**COAL COMBUSTION SCIENCE**
	TASK 2: DEPOSIT GROWTH AND PROPERTY DEVELOPMENT IN COAL-FIRED FURNACES
ORGANIZATION:	**Sandia National Laboratories, Livermore**
CONTRACT:	**FWP 0709**
REPORTING PERIOD:	**July 1 - Sept 30, 1994**
REPORTED BY:	**L. L. Baxter and D. R. Hardesty**
	Phone: (510) 294-2862 and (510) 294-2321

OBJECTIVES FOR TASK 2

Task 2 is a four-year project focused on the growth and properties of deposits generated in coal-fired furnaces. The project runs from Oct. 1993 to Sept 1997. The objectives of this research project are: (1) to provide a self-consistent database of simultaneously measured, time-resolved ash deposit properties in well-controlled and well-defined environments, and (2) to provide analytical expressions that relate deposit composition and structure to deposit properties of immediate relevance to PETC's Combustion 2000 program. This project is distinguished from other projects in the same research area by: (1) the development and deployment of *in situ* diagnostics to monitor deposit properties, (2) the time resolution of such properties during deposit growth, (3) simultaneous measurement of structural and composition properties, (4) development of algorithms from a self-consistent, simultaneously measured database that includes the interdependence of properties, and (5) application of the results to technologically relevant environments such as those being planned under the Combustion 2000 program. The deposit properties of principal interest in this project include the heat transfer coefficient, porosity, emissivity, tenacity, strength, density, and viscosity.

The first year is primarily associated with diagnostic development. This includes major activities associated with two *in situ*, real-time diagnostics for measuring inorganic materials on surfaces and in the gas-phase. Also, several diagnostics are being incorporated into the Sandia Multifuel Combustor (MFC) that will eventually be used to characterize ash deposit properties.

The research project is divided into six subtasks. The titles and objectives of these subtasks are summarized below, followed by a discussion of progress this quarter.

Subtask 2.1 Diagnostics for Coal Combustion Environments

The objective of this subtask is to develop and demonstrate diagnostics capable of *in situ* measurement of: (1) condensed-phase species on surfaces in combustion environments, and (2) inorganic vapors in turbulent, particle-laden, combustion gases.

Subtask 2.2 Experimental Determination of Transport, Thermal, and Structural Properties of Ash Deposits

The objective of this subtask is to provide self-consistent, simultaneous measurement of ash deposit properties under combustion conditions that simulate commercial-scale environments such as those expected to occur in Combustion 2000 technologies. Properties to be measured simultaneously and in real time include thermal conductivity, emissivity, porosity, mass and volume rate of growth, surface composition, and tenacity. Additional properties to be measured, but not in real time or *in situ*, include bulk elemental composition, bulk species composition, shear strength, true density, and detailed morphology.

Subtask 2.3 Analysis of Deposit Properties

The objective of this subtask is to provide an analytical capability for describing the development of deposit properties in combustion systems. Deposit properties to be predicted by this analytical method are similar to those discussed in Subtask 2.2 and include: (1) thermal conductivity, (2) emissivity, (3) porosity, (4) mass and volume rate of growth, (5) surface composition, (6) tenacity, (7) bulk elemental composition, and (8) major species composition.

Subtask 2.4 Chemical Reactions in Deposits

The objective of this subtask is to determine rates and mechanisms that describe chemical reactions in coal ash deposits that alter their properties or their morphology. This subtask is more limited in scope than the previous subtasks. We do not intend to conduct a comprehensive study of inorganic chemistry as it relates to ash deposits. We do intend to review available literature and perform calculations that allow us to capture the first-order terms that describe changes in deposit chemistry with time. This work will result in usable results, but is limited to global kinetics and simplified chemical mechanisms that outline the nature of the reactions and their dependence on operating parameters. The details of the kinetics will not be studied.

Subtask 2.5 Application to Combustion 2000 Program

The objective of this subtask is to exchange technology developed under other subtasks with ongoing Combustion 2000 efforts by other PETC contractors.

Subtask 2.6 Documentation

The objective of this subtask is to provide timely and accurate documentation of project progress, major milestones, and publishable results.

SUMMARY OF TECHNICAL PROGRESS DURING THIS QUARTER

Subtask 2.1 Diagnostics for Coal Combustion Environments

The emission FTIR spectroscopy diagnostic was used in collaboration with PSI Technology Inc. in support of their program to determine the effect of stoichiometry on oxidation state of iron in glass. The potential for using the new diagnostic to determine changes in iron oxidation states is

seen in the data of Fig. 2.1. The figure illustrates calculated emissivities for iron-containing minerals of several types. All raw data are taken from reference sources, and the emissivities are based on reflectance measurements from particulate layers containing particles ranging in size from 0-75 μm. Data for three minerals with iron in the Fe^{+2} state, one mineral with iron is mixed oxidation states, and one mineral with iron in the Fe^{+2} state are included.

Several observations can be made from Fig. 2.1. First, the presence of iron in any form raises the emissivity considerably. These emissivities are considerably higher than those for other minerals common to coal. Second, there are differences in the spectra, depending on the specific composition of the mineral grains. Third the differences tend to be subtle as determined by the emissivity of a feature exhibiting a difference of only 0.03 or so from that where no features exist.

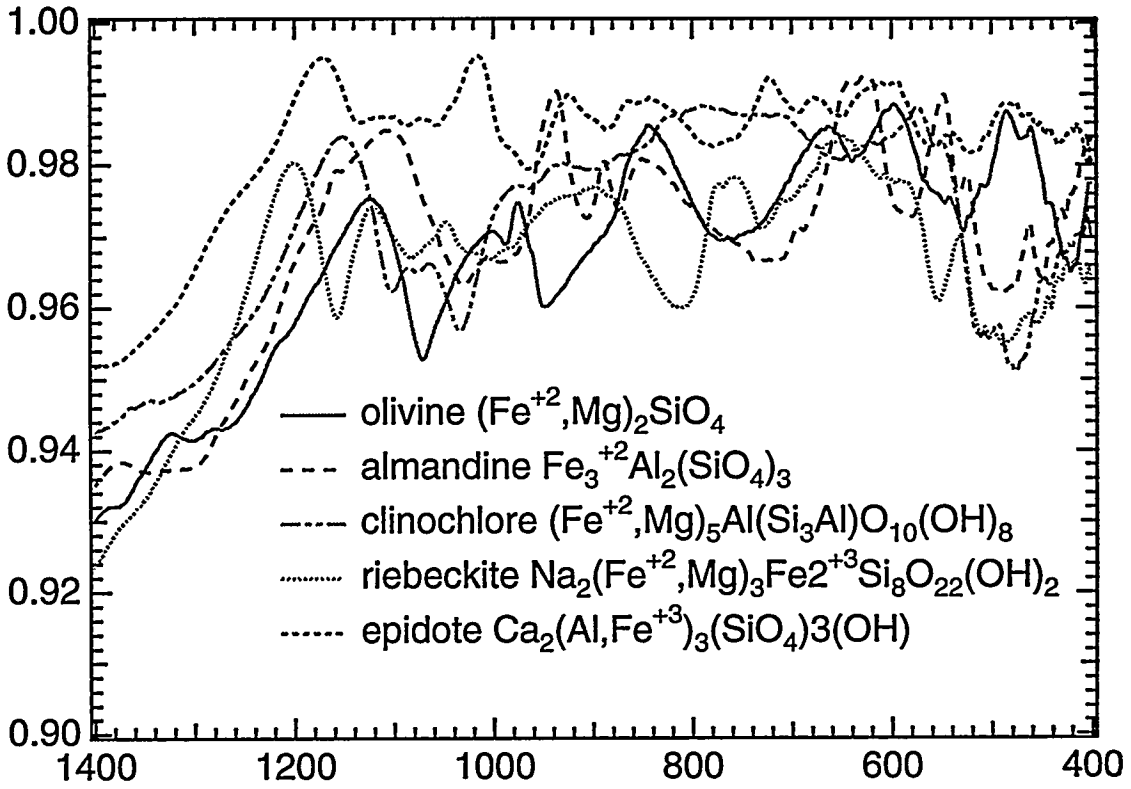

Figure 2.1 Spectral emissivities for iron-containing minerals in various oxidation states. Small differences in emissivity and complexity of spectra indicate that speciation of deposits from commercial systems containing such minerals will be challenging. Raw data are based on spectral reflectivities of particulate layers with particles ranging in size from 0-75 μm [Salisbury, et al., 1991].

Two samples of ash deposits on ceramic tubes from PSIT are under investigation at Sandia. Low resolution scans of the deposits have been completed, but analysis of the data has not. Higher resolution scans of the deposits are currently underway. The objective of the investigation is to determine the extent to which transitions from Fe^{+2}- to Fe^{+3}-based silicates can be observed using the emission technique. More detailed reports of this collaboration will be included in future quarterly reports.

The diode laser used in the previous MFC studies was found to tune over a very small range. During this quarter, we acquired and have installed three additional diode lasers from the manufacturer for evaluation. These lasers are currently under evaluation similar to that reported for the first laser in the last quarterly report. More detailed discussion of this work will appear in the future.

Subtask 2.2 Experimental Determination of Transport, Thermal, and Structural Properties of Ash Deposits

During this quarter, construction of the dynamic weighing device was completed and interfacing it with the data acquisition system was initiated. Also, a different sensor with approximately one order of magnitude more resolution was identified. It is a proprietary part of a commercial system, and we are currently making arrangements to buy one for use in our custom system. New slides and bearings for the optical thickness measuring device were also received this quarter. A complete discussion of these and the remaining diagnostics will be included, probably next quarter, when they are all completed and interfaced with the data acquisition system.

Subtask 2.3 Analysis of Deposit Properties

During this quarter, a theoretical approach to describing the reflectance and emittance of particulate layers was completed, and computer coding for the approach progressed significantly. The derivation of the approach is described in more detail below. It is divided into two broad discussions. The first is scattering of light by a single sphere and is essentially a generalization of Mie theory. The second is a discussion of the reflectance and emissivity of a particulate layer. The radiative transport equation, which describes radiative transport generally, is an integrodifferential equation with few known solutions of practical relevance. Under the assumptions that the layer is semi-infinite, isotropic, and that the particles are independent scatterers, a very good approximation to the general radiative transport equation can be derived. The solution depends on parameters describing the volume single scattering albedo. This is a material property that is related to single particle properties in unknown ways. We propose to approximate the relationship from the near-field and internal scattering properties of particles; We begin the technical portion of the discussion with the derivation of these quantities.

Generalization of Mie Theory

The objective of this portion of the discussion is to derive a description for the internal, near-field, and far-field scattering intensities for monochromatic, plane-wave light interacting with an isolated sphere of known optical properties. Traditional Mie theory describes the scattering intensities in the far-field. For our purposes, we need to understand light scattering in the near field and internal to the sphere. The development below follows that found in many standard texts, except that the

descriptions of the near and internal fields are not normally fully developed. Their development follows that of the far field except for some reasonably obvious differences. Some appreciation for the details of the derivation can be obtained from these standard texts. Two particularly readable texts [Bohren and Huffman, 1983; Kerker, 1969] form the basis of this discussion.

The point of departure in the derivation of the scattering of light is Maxwell's equations, which can be expressed as the divergence of electric and magnetic vectors

$$\nabla \bullet \mathbf{D} = \rho \tag{2.1}$$

and

$$\nabla \bullet \mathbf{B} = 0 \tag{2.2}$$

and the curl of related electric and magnetic vectors, expressed as

$$\nabla \times \mathbf{E} = -\frac{\partial \mathbf{B}}{\partial t}, \tag{2.3}$$

and

$$\nabla \times \mathbf{H} = \mathbf{J} + \frac{\partial \mathbf{D}}{\partial t}. \tag{2.4}$$

Equation 2.1 indicates that the divergence of electric displacement (**D**) is everywhere zero except at point sources and sinks. If such point sources and sinks are present and are represented by a charge density (ρ), the field lines tend to diverge or converge from them. Equation 2.2 indicates that the divergence of the magnetic induction (**B**) is everywhere zero, with no similar point sources or sinks (i.e., magnetic monopoles do not exist). Equation 2.3 indicates that a time-varying magnetic induction gives rise to an electric field (**E**), with the field lines of the latter curling around the field lines of the former. Equation 2.4 indicates that both time varying electric displacement and electric current density (**J**, time varying or steady) give rise to magnetic fields (**H**) with field lines of the latter curling around those of both the current density and the electric displacement.

To a reasonable approximation, **J**, **D** and **H** relate to **B** and **E** in simple ways. The current density is proportional to the electric field;

$$\mathbf{J} = \sigma \mathbf{E}. \tag{2.5}$$

The electric displacement is similarly proportional to the electric field.

$$\mathbf{D} = \varepsilon \mathbf{E}, \tag{2.6}$$

The proportionality constants σ and ε represent the conductivity and a combination of the electric susceptibility and permittivity, respectively. Both are material properties; The latter may be a complex number.

The magnetic induction is similarly proportional to the magnetic field, with the proportionality constant being the permeability, another material property that is commonly assumed to be constant for all materials in the application of Mie theory.

$$\mathbf{B} = \mu\mathbf{H}. \tag{2.7}$$

These can be rearranged, with modest assumptions about physical properties of materials, to yield vector wave equations as follows:

$$\nabla^2\mathbf{E} + k^2\mathbf{E} = 0, \tag{2.8}$$

assuming there are no free charges, and

$$\nabla^2\mathbf{H} + k^2\mathbf{H} = 0. \tag{2.9}$$

Both fields can also be assumed to be divergence free. In addition, the cross product of either field is proportional to the other field.

These linear, vector, differential equations can be reduced to scalar wave equations if we assume the presence of a vector **M** with the following properties.

$$\mathbf{M} = \nabla \times \mathbf{c}\psi \tag{2.10}$$

where **c** is an arbitrary constant vector and ψ is a scalar function. It follows that

$$\nabla^2\mathbf{M} + k^2\mathbf{M} = \nabla \times \left[\mathbf{c}\left(\nabla^2\psi + k^2\psi\right)\right]. \tag{2.11}$$

If a second vector **N** is defined relative to **M** as follows

$$\mathbf{N} = \frac{\nabla \times \mathbf{M}}{k} \tag{2.12}$$

then

$$\nabla^2\mathbf{N} + k^2\mathbf{N} = 0 \tag{2.13}$$

Therefore, these two new vectors solve the vector wave equation if the scalar function ψ solves the scalar wave equation

$$\nabla^2\psi + k^2\psi = 0. \tag{2.14}$$

In spherical coordinates, this function is given by

$$\frac{1}{r^2}\frac{\partial}{\partial r}\left(r^2\frac{\partial\psi}{\partial r}\right) + \frac{1}{r^2\sin\theta}\frac{\partial}{\partial\theta}\left(\sin\theta\frac{\partial\psi}{\partial r}\right) + \frac{1}{r^2\sin\theta}\frac{\partial^2\psi}{\partial\phi^2} + k^2\psi = 0 \tag{2.15}$$

If we assume that Ψ is separable into three factors, each dependent on one coordinate, we have

$$\psi(R,\theta,\phi) = R(R)\Theta(\theta)\Phi(\phi). \tag{2.16}$$

This yields three ordinary differential equations of the form

$$\frac{d^2}{dr}\left(r^2\frac{dR}{dr}\right)+\left[k^2r^2-n(n+1)\right]R=0, \tag{2.17}$$

$$\frac{1}{\sin\theta}\frac{d}{d\theta}\left(\sin\theta\frac{d\Theta}{d\theta}\right)+\left[n(n+1)-\frac{m^2}{\sin^2\theta}\right]\Theta=0, \tag{2.18}$$

and

$$\frac{d^2\Phi}{d\phi^2}+m^2\Phi=0. \tag{2.19}$$

All three are classical ordinary differential equations with well known solutions. The solutions are the spherical Bessel functions, the associated Legendre functions, and complex exponential (sine/cosine) functions, respectively. The solutions represented by all finite values of m, and n are linearly independent and form a basis set which can be used to describe the solution to the wave equation. The task from this point is to determine determining the coefficients of each of the components of this basis set.

It is at this point that our approach diverges from the traditional solution to Mie theory. Traditionally, Mie theory describes the far-field scattering of light from a sphere. We seek that solution and the near field and internal scattering fields.

The scalar ψ, and therefore the vectors **M** and **N**, can be divided into even and odd components as follows

$$\mathbf{M}_{emn} = \nabla\times(\mathbf{r}\psi_{emn}) \tag{2.20}$$

$$\mathbf{M}_{omn} = \nabla\times(\mathbf{r}\psi_{omn}) \tag{2.21}$$

$$\mathbf{N}_{emn} = \frac{\nabla\times\mathbf{M}_{emn}}{k} \tag{2.22}$$

$$\mathbf{N}_{omn} = \frac{\nabla\times\mathbf{M}_{omn}}{k} \tag{2.23}$$

These vectors form the basis for infinite series descriptions in m and n of the incident, scattered, and internal fields in a spherical particle. Most of the coefficients of the series can be shown to be zero. The internal fields simplify to

$$\mathbf{E}_1 = \sum_{n=1}^{\infty} i^n E_o \frac{2n+1}{n(n+1)} \left(c_n \mathbf{M}_{o1n}^{(1)} - i d_n \mathbf{N}_{e1n}^{(1)} \right) \tag{2.24}$$

and

$$\mathbf{H}_1 = \frac{-k_1}{\omega \mu_1} \sum_{n=1}^{\infty} i^n E_o \frac{2n+1}{n(n+1)} \left(d_n \mathbf{M}_{e1n}^{(1)} - i c_n \mathbf{N}_{o1n}^{(1)} \right) \tag{2.25}$$

and the scattered fields simplify to

$$\mathbf{E}_s = \sum_{n=1}^{\infty} i^n E_o \frac{2n+1}{n(n+1)} \left(i a_n \mathbf{M}_{e1n}^{(3)} - b_n \mathbf{N}_{o1n}^{(3)} \right) \tag{2.26}$$

and

$$\mathbf{H}_s = \frac{k}{\omega \mu} \sum_{n=1}^{\infty} i^n E_o \frac{2n+1}{n(n+1)} \left(i b_n \mathbf{M}_{o1n}^{(3)} - a_n \mathbf{N}_{e1n}^{(3)} \right) \tag{2.27}$$

The superscripts (1) and (3) indicate that the spherical Bessel functions of first and third kind, respectively, are used to describe the radial dependence in ψ. All other terms have been defined except the coefficients a_n, b_n, c_n, and d_n. These are given by

$$a_n = \frac{m\vartheta_n(mx)\vartheta_n'(x) - \vartheta_n(x)\vartheta_n'(mx)}{m\vartheta_n(mx)\xi_n'(x) - \xi_n(x)\vartheta_n'(mx)} \tag{2.28}$$

$$b_n = \frac{\vartheta_n(mx)\vartheta_n'(x) - m\vartheta_n(x)\vartheta_n'(mx)}{\vartheta_n(mx)\xi_n'(x) - m\xi_n(x)\vartheta_n'(mx)} \tag{2.29}$$

$$c_n = \frac{\vartheta_n(x)\xi_n'(x) - \xi_n(x)\vartheta_n'(x)}{\vartheta_n(mx)\xi_n'(x) - m\xi_n(x)\vartheta_n'(mx)} \tag{2.30}$$

$$d_n = \frac{m\vartheta_n(x)\xi_n'(x) - m\vartheta_n(x)\vartheta_n'(x)}{m\vartheta_n(mx)\xi_n'(x) - \xi_n(x)\vartheta_n'(mx)} \tag{2.31}$$

where x is the size parameter and ϑ is related to the spherical Bessel function of the first kind as

$$\vartheta_n(y) = y\, j_n(y) \tag{2.32}$$

and ξ is related to the spherical Bessel function of the third kind as

$$\xi_n(y) = y\, h_n^{(1)}(y). \tag{2.33}$$

This completes the mathematical description of light scattering by a particle with internal and external fields described for all radial positions. These results will be used in the reflectivity/emissivity model of a particulate surface. Most of the details of the solution have been omitted but can be found (for the case of scattering in the far field) in reference texts. The calculation of the results is not trivial, involving several considerations of convergence, rounding error, recursion, and precision.

During this quarter, we completed coding of the far-field scattering portion of the code (series in a_n and b_n) in C++ with the intent to make use of object-oriented programming techniques in the calculation of the reflectivity and emissivity. The code is debugged and results have been compared with available published results. They agree within rounding error. This code is useful in its present form as a traditional Mie scattering code, and the listing is included in the appendix. It was written using the Symantec C++ compiler on a Macintosh.

While currently a useful code, there are other, mainly FORTRAN, codes that perform similar calculations. Our intention is to make calculations of the internal and near-field scattering patterns that are not available from existing codes. We have not yet completed coding of the internal-or near-field portion of the code. We are also unaware of any available reference data with which to compare these calculations. The internal field is more complicated to compute and display since it exhibits strong radial variation. Traditional scattering calculations assume far field measurements with no radial variation, i.e., the scattering intensity in a given solid angle does not depend on distance from the particle. The light intensity at a point, as opposed to within a solid angle, depends on distance from the particle.

An example of the calculated results from our code is shown in Fig. 2.2. Scattering patterns for plane, unpolarized light with a wavelength of 0.6328 μm interacting with a particle with a complex index of refraction of (1.33, 1.0e-8) are illustrated for a 0.5 and 5 μm particle. These conditions correspond to a water droplet illuminated by a HeNe laser beam. The scattering pattern is illustrated on a log scale covering slightly over 6 orders of magnitude. The intensities are normalized to the overall scattering efficiencies of the particles such that the forward scattered intensity of the small particle exceeds that of the large particle by the ratio of their scattering efficiencies. The diagram indicates the relative intensities of the scattered light. For example, light scattered at 90°C from the direction of the incident beam is 2.5 orders of magnitude less intense than light scattered along the forward axis for the 0.5 μm particle. The beam travels in the direction of 0°. Data for the 0.5 μm particle are illustrated on bottom whereas data for the 5 μm particle are illustrated on top. Both scattering patterns are symmetrical about the horizontal axis, but only half of each is illustrated.

The diagram illustrates how small particles scatter more light at wide angles than large particles. The large particle in this case has a scattering efficiency of about 2, whereas the small particle's scattering efficiency is approximately 3.6. These significant differences in particle behavior as a function of size introduce particle size effects in particulate layers as well. An indication of this change is gained from the data illustrated in Figure 2.3 [Salisbury, et al., 1991], where the spectral emissivities from particulate samples of two reagent grade minerals are displayed. One spectrum isfrom large sized mineral grains (75-250 μm) whereas the second is from smaller mineral grains

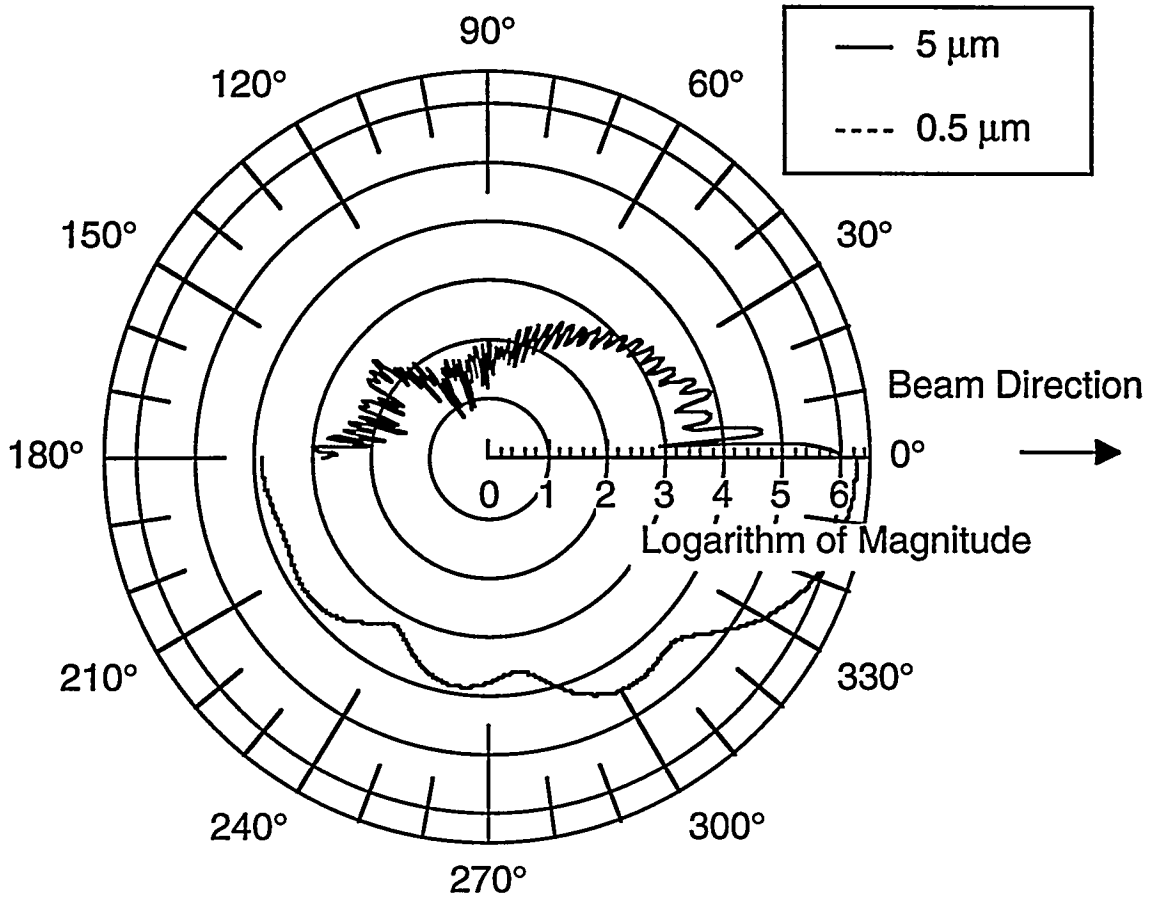

Figure 2.2 Scattering diagram for two particles/droplets with identical optical properties but different sizes. Scattering intensities are shown on logarithmic scale and angles are shown in degrees. Both particles produce symmetrical patterns around an angle of 0°. Only half of the symmetrical pattern is illustrated.

(0-75 μm). Over most of the range of wavenumbers, the smaller particles exhibit lower emissivities, consistent with their higher backscattering efficiencies. The features in both spectra between 3600 and 3300 wavenumbers are hydroxyl bands that are associated with either adsorbed moisture or impurities in the material. The remaining features are associated with jadeite.

A quantitative description of these effects is being developed, as is discussed in the following section. Note that there are several considerations, in addition to particle size, that determine the spectral emissivity properties of particulate layers.

Reflection and Emission from a Particulate Layer

This section of the discussion describes emission and reflection from a particulate layer assuming the behavior of an individual particle in that layer is known. The scattering of a particle that has near neighbors differs from that of an isolated particle – sometimes by large amounts. An

appreciation for the different behaviors can be quickly acquired by considering the large particle size limit of scattering efficiencies. It is well known that particles scatter twice the amount of light as is incident on their geometric cross section as the particle size becomes large. At smaller sizes, the amount of scattering may either exceed a factor of two (sometimes by a large margin), or approach zero.

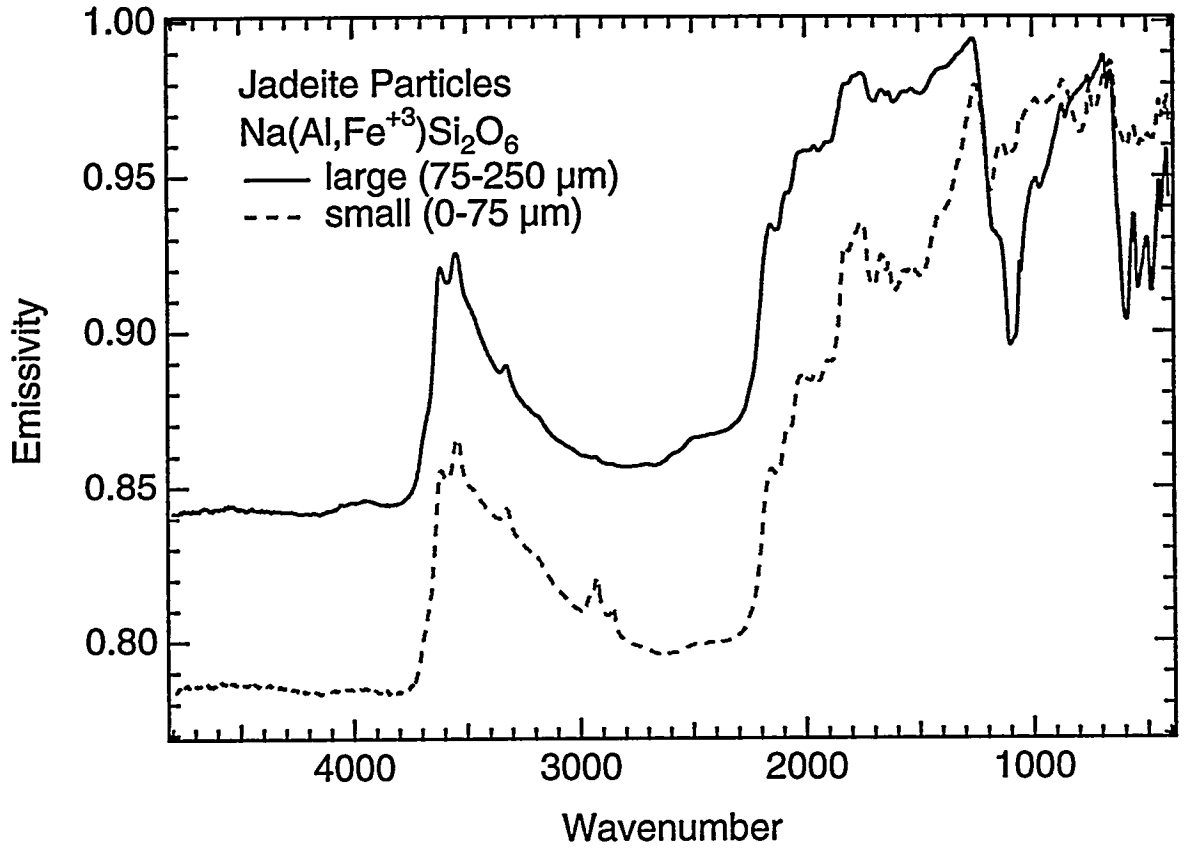

Figure 2.3 Spectral emissivities for particulate layers illustrating the effect of particles size on overall emissivity.

If particles in close proximity behaved similarly, they would, as a group, scatter twice the light as is incident on the layer. This violates conservation of energy principles. Clearly, the presence of other scatterers in the vicinity of a particle influences the particles' scattering behavior. The results of the previous section describe the scattering patterns at arbitrary distance from the particle. This provides a means of approximating the scattering of light by particles imbedded in a particulate layer.

The radiative transport equation is the point of departure for describing radiative transfer through arbitrary media

$$\frac{\partial\ I(s,\Omega)}{\partial s} = -E(s,\Omega)I(s,\Omega) + \frac{1}{4\pi}\int_{4\pi} I(s,\Omega')G(s,\Omega,\Omega')d\Omega' + F(s,\Omega) \tag{2.34}$$

where I represents the radiance of a beam, s represents distance of pathlength, Ω represents direction, E represents the volume extinction coefficient, G represents the volume angular scattering coefficient, and F represents the volume emission coefficient.

By contrast to the wave equation discussed in the previous section, this integrodifferential equation does not lend itself to solution by systematic means. The ad hoc solutions that do exist are not of particular practical relevance. The equation can be simplified somewhat for the case of horizontally stratified media, but it does not reduce to a form that has a known general analytical solution.

If we assume the particulate layer is semi-infinite and homogeneous, a solution to the radiative transport equation follows from an analysis of scattering in the media. Under these assumptions, it should make no difference to the emissivity or reflectivity if a thin layer of particles is added or removed from the surface of the layer. The solution to the equation is found by requiring that the expression for the reflectance and emission from the original layer be equal to that of the surface after the layer is removed. Fig. 2.4 illustrates the situation for the case of the bidirectional reflectance. The five first-order changes in the reflectance associated with adding a thin layer of particles to the surface are illustrated as (a) reduction in intensity by extinction of the light as it passes through and returns through the layer; (b) scattering of the new layer toward the observer; (c) light scattered from the new layer being backscattered from underlying material; (d) light scattered from the lower medium illuminating the new layer and adding to the observed reflectance; and (e) light twice scattered between the new layer and the original layer illuminating the old layer. The sum of these five effects must be zero.

Within the constraints of isotropic, independent scatterers (the assumptions of this analysis), the radiative transport equation yields an exact solution given by

$$r(i,e,g) = \frac{w}{4\pi}\frac{\mu_o}{\mu_o + \mu}H(\mu_o)H(\mu) \tag{2.35}$$

where

$$H(x) = 1 + \frac{w}{2}xH(x)\int_0^1 \frac{H(x')}{x + x'}dx' \tag{2.36}$$

and i, e, and g represent the zenith angles of incidence and emergence (observation), and the phase angle, respectively, w represents the single-scattering albedo, and μ and μ_o represent the cosines of e and i, respectively.

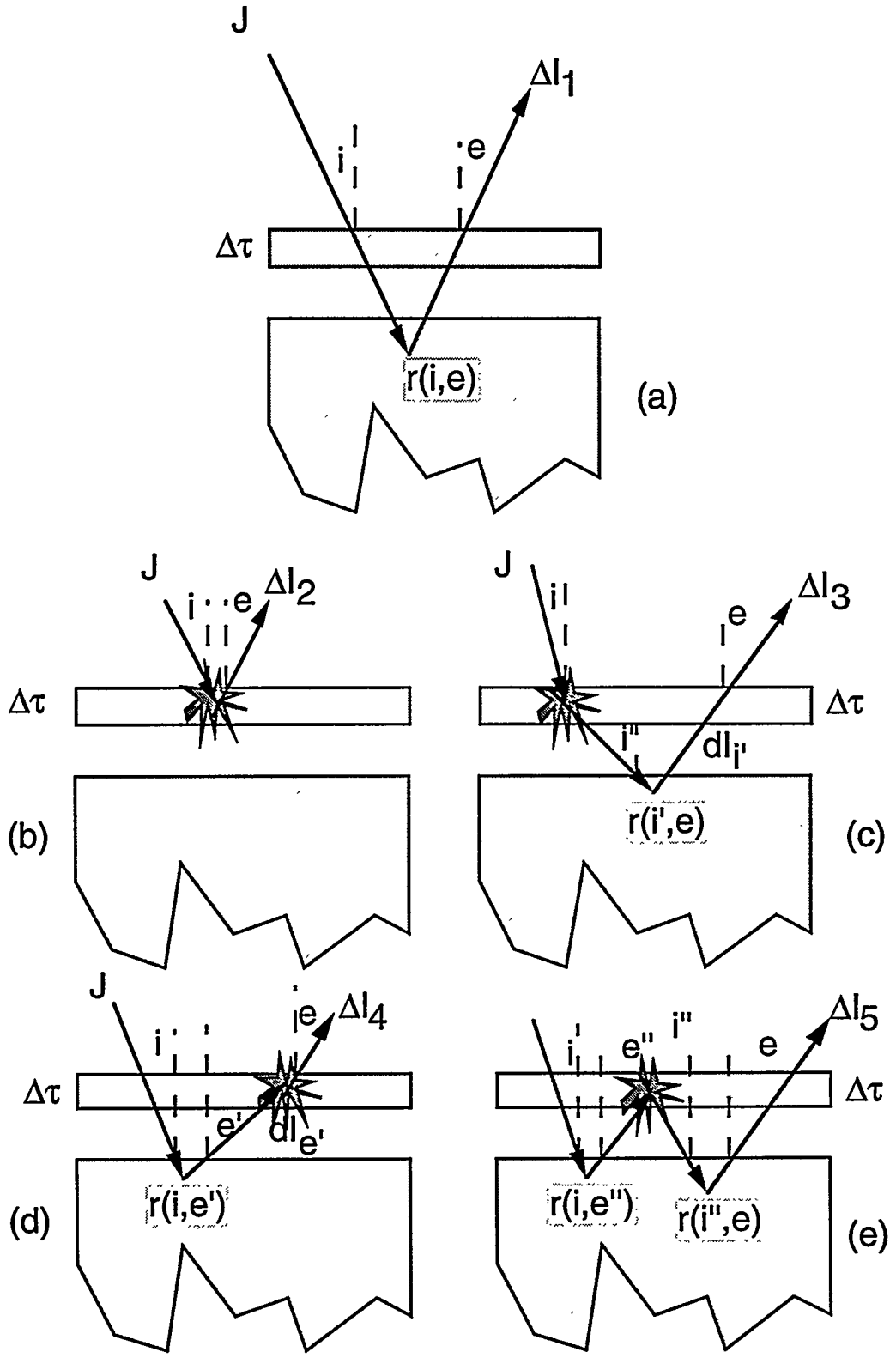

Figure 2.4 Schematic illustration of the solution of the radiative transport equation.

The function H is obviously somewhat awkward to calculate, but it is analytical and there are several good approximations to it. The surface emissivity can be similarly derived or calculated by difference from the incident beam and the reflectivity. The problem of computing the reflectivity or emissivity has been reduced to calculation of the parameter w and geometrical quantities.

There remain some additional issues in the calculation of the reflectance and emittance. These include a surge in brightness at near-back-scattered angles associated with shadow hiding, the effects of collections of non-identical particles either in size or scattering properties, and the generalization of the results to emission. There are means of addressing all of these issues that are currently being pursued. The only remaining material prameter is w. We intend to evaluate this approach to calculating spectral emissivities and reflectivities as an alternative to our first-order model recently published [Richards, et al., 1994].

Subtask 2.4 Chemical Reactions in Deposits

No work was scheduled or performed during this quarter on this subtask.

Subtask 2.5 Application to Combustion 2000 Program

During this quarter, arrangements were made with Combustion 2000 contractors to investigate materials compatibility issues related to their objectives in the HITAF project. Surface corrosion of high-performance ceramics proposed for use in heat exchangers is of concern. SiC is a leading material being considered for this application.

Dr. Dan Seery of United Technologies has indicated particular interest in the high-temperature performance of β silicon carbide and suggested Coors Ceramics as a supplier. We have obtained two samples of the material from Coors and have agreed with Dr. Seery on a scope and statement of work appropriate for his program. The outline of the research to be performed is indicated below.

SiC Corrosion Investigation

Objective

The objective of this project is to determine the high-temperature corrosion mechanisms of silicon-carbide-based ceramics under conditions similar to those in advanced coal combustors (Combustion 2000 HITAF systems, for example).

Scope

The initial scope of the project will involve modest efforts using existing equipment and samples procured from leading silicon carbide manufacturers. We will confer with Combustion 2000 contractors to identify the proper material and conditions. Experiments will be limited to short duration (3 hour) tests of two samples in Sandia's Multifuel Combustor (MFC) Laboratory. The anticipated results include: (1) in situ, real-time, nondestructive observation of the transition from silicon carbide to silica on the surface of the ceramic upon exposure to high-temperature (1000 °C)

oxidizing gases; and (2) similar observations of the transition from silica to alkali-silicate material on the surface upon addition of non-condensing alkali salts to the gas stream.

Relevance

This work should demonstrate that the anticipated corrosion of silicon carbide is not dependent upon the formation of a condensed alkali-containing material on the surface of the ceramic, as has been proposed by leading researchers in the field. Rather, such corrosion can occur by direct reaction of gas-phase alkali and condensed-phase silica. The practical ramification is that the rate of corrosion should not be expected to decrease as the surface temperature increases beyond the dew point of the alkali-containing gases. Such a decrease has been postulated by other laboratories.

Approach

Samples of appropriate silicon carbide will be exposed to the high-temperature environment of the MFC. Recently developed FTIR emission spectroscopy instrumentation will be used to monitor the composition of the surface. Samples will initially be exposed to an oxidizing stream containing no alkali. Sample surface temperatures will be held at about 1000 °C, safely above the thermodynamically stable region of alkali sulfates (≈ 800 °C). After the silica surface layer is observed, alkali (NaCl) will be added to the vitiated flow of the MFC, and the transition of the silica layer to an alkali silicate layer will be monitored using the same emission spectroscopy diagnostic. After the test, the samples will be prepared for examination under an SEM microscope, either at Sandia or at one of our collaborator's laboratories, where personnel who traditionally perform materials assessments in this manner are available. We will also work with other departments within Sandia to see what value can be added by our corrosion/materials/ceramics experts.

Schedule

We plan to complete this work by the end of CY94 under our existing PETC budget.

Subtask 2.6 Documentation

Papers and reports submitted under this contract this quarter are summarized separately below. Presentations regarding this work were made at the Annual Contractor's review meeting, at the EPRI Conference on the Effect of Coal Quality on Power Plants, and at the 25th Symposium (International) on Combustion. Copies of slides from the presentation at the Contractor's Review Meeting were mailed to Chuck Garrett, at his request.

PLANS FOR NEXT QUARTER

During the next quarter, the new tunable diode lasers will be characterized and a sample cell will be used to verify their application to alkali vapors in a clean environment. The proper lasers will be selected for further use on the project. The first phase of the emission FTIR spectroscopy analyses

of iron-containing glasses will be completed. The theoretical description of the emissivity of particulate layers will also be completed.

ACKNOWLEDGMENTS

Sandia Contributors

Gian Sclippa and Al Salmi are instrumental in operating and maintaining the MFC and in assisting in the design and construction of diagnostic and probe equipment as well as conducting TDL experiments.

Industrial Contributors

Many of the chemical and physical analyses of solid samples of fly ash, deposits, and raw coal gathered during this investigation are performed by CONSOL Inc. with the assistance of Murray Abbott, Vince Conrad, and Diane Havekotte.

Academic Contributors

Mr. Galen Richards (Graduate Student, BYU) completed much of his PhD experimental work performing the FTIR measurements in the MFC and providing SEM images for analysis. He completed his PhD during the last quarter. Prof. John Harb (Brigham Young University) is his graduate advisor and collaborator in these efforts. Prof. Peter Bernath (Universities of Waterloo and Arizona) and Postdoctoral Associate Dr. Ram Ram (Univ. of Arizona) are collaborating in the collection and analysis of inorganic vapor species compositions at high temperature. Prof. Bryan Jenkins (UC Davis) assists in many aspects of experimental and theoretical work. His contributions are primarily on other projects, but collateral contributions to this project, in particular the work on the deposit thickness measurement, are gratefully acknowledged. Ms. Janell Bloyd (HS Teacher) and Alex Valle (HS student) worked on data acquisition and gas analysis systems, respectively. This quarter, Mr. Peter Adams (Cornell) started work in the MFC, with initial tasks relating to operation of the emission FTIR diagnostic.

PUBLICATIONS, PAPERS, AND PRESENTATIONS

The following presentations and papers based in whole or in part on PETC-supported work were completed in the last quarter.

Baxter, L.L., "Deposit Formation and Property Development During Pulverized Coal Combustion," presented and published in the proceedings of the Ninth Annual Contractor's Review Meeting, Pittsburgh, PA, July, 1994.

Baxter, L.L., G.H. Richards, and J.H. Harb, "Application of advanced technology to ash-related problems in boilers," presented and published in the proceedings of the EPRI Conference on the Effect of Coal Quality on Power Plants, Charleston, SC, Aug. 1994.

Richards, G.H., J. H. Harb, L. L. Baxter, S. Bhattacharaya, R. P. Gupta, and T. F. Wall, "Radiative Heat Transfer in Pulverized-Coal-Fired Boilers -- Development of the Absorptive/Reflective Character of Initial Ash Deposits," presented at the Twenty-Fifth Symposium (International) on Combustion, July 31- August 5, 1994.

REFERENCES FOR TASK 2

Bohren, C. F., and Huffman, D. R. (1983). *Absorption and Scattering of Light by Small Particles.* New York: John Wiley & Sons.

Kerker, M. (1969). *The Scattering of Light and Other Electromagnetic Radiation.* New York: Academic Press.

Richards, G. H., Harb, J. N., Baxter, L. L., Bhattacharya, S., Bupta, R. P., and Wall, T. F. (1994). "Radiative Heat Transfer in PC-Fired Boilers — Development of the Absorptive/Reflective Character of Initial Ash Deposits on Walls". In *Twenty-Fifth Symposium (International) on Combustion,* . Irvine, CA: The Combustion Institute.

Salisbury, J. W., Walter, L. S., Vergo, N., and D'Aria, D. M. (1991). *Infrared (21.-25 μm) spectra of minerals.* Baltimore: Johns Hopkins University Press.

SCHEDULE AND MILESTONES FOR TASK 2

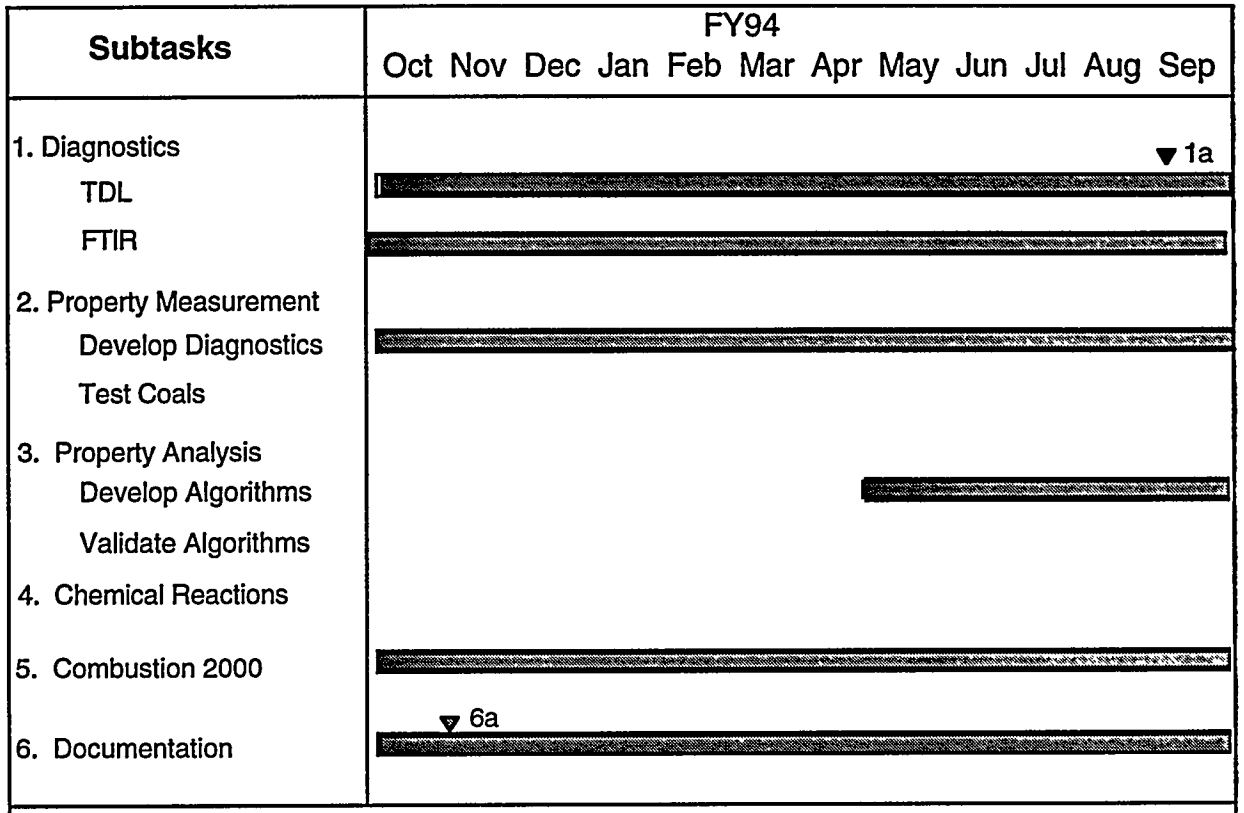

Milestones

1a First TDL results obtained from the MFC.

6a. Completion of three Topical Reports with submission for PETC review.

Task 2 Appendix

During this quarter, we completed coding of the far-field scattering portion of a computer code in C++ with the intent to make use of object-oriented programming techniques in the calculation of the reflectivity and emissivity. The code is debugged and results have been compared with available published results. They agree within rounding error. This code is useful in its present form as a traditional Mie scattering code, and the listing is included in the appendix. It was written using the Symantec C++ compiler on a Macintosh. No attempt has been made to make it portable. The only known portability issue has to do with the dynamic memory allocation using handles. Handles, as implemented on the Macintosh, are not generally portable to other computers.

The program listing follows. The program reads a ASCII text file entitled Mie.in and writes a similar file entitled Mie.out. The total scattering, and extinction, and backscattering efficiencies are calculated together with the angularly resolved scattering matrix. The latter allows determination of the scattering pattern for arbitrarily polarized light. The input data include the complex indices of refraction for both the particle and the medium, the particle diameter, the wavelength of light incident on the particle, and the resolution for the angular scattering patterns. Typical input and output files are shown, with low angular resolution to preserve space. Note that the scattering, extinction, and backscattering efficiencies are only written to the screen, not the output file. The output file is intended for plotting purposes.

The portion of the code shown below is fully functional and, so far as is known, bug free. It will be part of a larger code that will predict the internal and near-field results and, ultimately, scattering from a particulate layer. There has been no attempt to make the version illustrated below user friendly to the point of having graphical user interfaces, etc.

Code Listing

```
/* This program calculates the directional scattering of monochromatic
light from a spherical particle as a function of optical properties,
angle, particle size, and wavelength of incident beam.  The incident
beam is assumed to be a plane wave and the computed scattering intensities
are appropriate for the far field. The medium is assumed to be nonabsorbing.

Copyright 1994 by Larry L. Baxter
All Rights Reserved  */
```



```
/* Include Files */
#include <iostream.h>
#include <complex.h>
#include <stdlib.h>
#include <iomanip.h>
#include <fstream.h>
```

```
/* Template Functions */

template <class T, class N>
/* This template allocates a handle to an array of size given by 'size' and
type given by the type of 'value1'. The array is initialized to the value of
value1. */
T **dynalloc(N size, T value1)
 {
  T **Hndl;
  N idum;

   if ((Hndl=(T **)calloc(size, sizeof(T *)))==0)
   {
    cout << "Unable to allocate membor for array of pointers. \n";
    return(0);
   }
  for (idum = 0 ;idum < size; idum++)
   {
     if ((Hndl[idum]=(T *)calloc(1,sizeof(T))) == 0)
     {
      cout << "Unable to allocate memory for array T[" << idum << "].\n";
      return(0);
     }
    else
     {
       *Hndl[idum] = value1;
     }
   }
  return(Hndl);
 }

template <class T, class N>
void dyndest(N size, T **Hndl)
  {
  N idum;

   for (idum = 0;idum < size; idum++)
    {
     free(Hndl[idum]);
    }
   free(Hndl);
```

```
   return;
  }

/*  Function  Prototypes  */

short maxord(double szp, complex rfirel);
short logder(short mxord, double szp, complex rfirel, complex **d);
double ricbes(short ndiv, short mxord, double x,
   complex refrel, complex **d, complex **s1, complex **s2);

/*   Main Listing */

void main()
   {
   const double PI = 3.14159265;
   complex rfirel, rfimed, rfipart, cdum;
   double radp,wavel,szp,dndiv,qsca,qext,qback,s11nor,s11,s12,s33,s34,pol,ang;
   short idum;
   short mxord, ndiv;
   complex **d, **s1, **s2;

/ *    Collect input parameters rfimed, rfipart, radp, wavel, and ndiv.  Calculate
   derived parameters rfirel, szp, and dndiv. */

/ /    cout << "Enter complex refractive indices for the medium and particle. \n";
/ /    cin >> rfimed >> rfipart;
   ifstream inMieFile("Mie.in", ios::in);
   if (!inMieFile) cerr << "File Mie.in could not opened." << endl;

   inMieFile >> rfimed >> rfipart;
   inMieFile >> radp >> wavel;
   inMieFile >> ndiv;
   inMieFile.close();
/ /    rfimed = complex(1.0,0.0);
/ /    rfipart = complex(1.55,0.0);
   rfirel = rfipart/rfimed;
/ /    cout << "Enter particle radius and radiation wavelength (in same units).\n";
/ /    cin >> radp >> wavel;
/ /    radp = 0.525;
/ /    wavel = 0.6328;
   szp = 2.0*PI*radp*real(rfimed)/wavel;
/ /    cout << "Enter number of angles in 0-90° over which to compute results.\n";
/ /    cin >> ndiv;
```

```
// ndiv = 21;
   dndiv = PI/2.0/(ndiv-1);
/* Determine maximum order of function required and allocate memory
(dynamically)
   for the d, s1, and s2 pointers. */
   mxord = maxord( szp, rfirel);
/* Allocate dynamic memory for large arrays. */
   cdum = 0.0;
   d = dynalloc(mxord, cdum);
   s1 = dynalloc(short(2*ndiv-1), cdum);
   s2 = dynalloc(short(2*ndiv-1), cdum);
/* Compute the values of the log-derivative function d. */
   idum = logder(mxord, szp, rfirel, d);
/* Calculate the scattering, extinction, and back-scattering cross sections.
*/
   qsca = ricbes(ndiv, mxord, szp, rfirel, d, s1, s2);
   qext = (4.0/(szp*szp))*real(**s1);
   qback = (4.0/(szp*szp))*abs(**(s1+2*ndiv-2))*abs(**(s1+2*ndiv-2));
   cout << "qsca, qext, and qback = " << qsca << " " << qext << " " << qback << endl;
   cout << endl;
   cout.width(14);
   cout.setf(ios::showpoint | ios::stickywidth);
/* Calculate the scattering matrix and polarity parameters. */
   s11nor = 0.5*(pow(abs(**s2),2.0)+pow(abs(**s1),2.0));
   cout << "ang " << "s11 " << "s33 " << "s34 " << "pol " << endl;
   cout << endl;
   ofstream outMieProg("Mie.out");
   if (!outMieProg) cout << "File could not be opened" << outMieProg << endl;
   if (outMieProg) outMieProg << "ang" << "\t" << "s11" << "\t" << "s33" <<
   "\t" << "s34" << "\t" << "pol" << endl;
   for (idum = 0; idum<2*ndiv-1; idum++)
      {
      s11 = 0.5*(pow(abs(**(s1+idum)),2)+pow(abs(**(s2+idum)),2));
      s12 = 0.5*(pow(abs(**(s2+idum)),2)-pow(abs(**(s1+idum)),2));
      s33 = real(**(s2+idum)*conj(**(s1+idum)))/s11;
      s34 = imag(**(s2+idum)*conj(**(s1+idum)))/s11;
      pol = -s12/s11;
      s11 = s11/s11nor;
      ang = 180.0/PI*dndiv*idum;
      cout << setprecision(3) << ang << setprecision(7) << s11 <<
        s33 << s34 << pol << endl;
      if (outMieProg) outMieProg << ang << "\t" << s11 << "\t" <<
        s33 << "\t" << s34 << "\t" << pol << endl;
```

```
      }
   outMieProg.close();
   dyndest(mxord, d);
   dyndest(short(2*ndiv-1), s1);
   dyndest(short(2*ndiv-1), s2);
   }

short maxord( double szp, complex rfirel)
   {
   complex y;
   double xstp,ystp;
   short mx;

   y = szp*rfirel;
   xstp = szp+4.0*pow(szp,float(1/3))+2;
   ystp = abs(y);
   if (ystp > xstp)
      mx = ceil(ystp);
   else
      mx = ceil(xstp);
   return(mx+15);
   }

short logder(short ord, double szp, complex rfirel, complex **d)
   {
   complex y;
   long idum;

   y = szp*rfirel;

   for (idum = ord-2 ; idum >= 0 ; idum--)
      {
      **(d+idum) = (idum+2)/y-1.0/(**(d+idum+1)+(idum+2)/y);
      }
   idum = 1;
   return(idum);
   }

double ricbes(short ndiv, short mxord, double x,
complex refrel, complex **d, complex **s1, complex **s2 )
   {
   const double PI = 3.14159265;
   double psi, psi0, psi1, chi, chi0, chi1, qsca, fn;
```

```
    complex xi0, xi1, an, bn;
    long idum, idum2, n;
    short it, p;
    complex xi;
    double **pi0, **pi1, **pi, **tau, **amu;


//  Large arrays are allocated on the heap

    psi = 0.0;
    psi1 = 1.0;
    pi = dynalloc(ndiv, psi);
    pi0 = dynalloc(ndiv, psi);
    pi1 = dynalloc(ndiv, psi1);
    tau = dynalloc(ndiv, psi);
    amu = dynalloc(ndiv, psi);
//    Initialize amu;
    for (idum = 0; idum < ndiv; idum++)
       {
       **(amu+idum) = cos(idum*PI/2.0/(ndiv-1));
       }
    psi0 = cos(x);
    psi1 = sin(x);
    chi0 = -psi1;
    chi1 = psi0;
    xi0 = complex(psi0,-chi0);
    xi1 = complex(psi1,-chi1);
    qsca = 0.0;
    for (n=1; n < mxord; n++)
       {
       fn = (2.0*n+1.0)/(n*(n+1.0));
       psi = (2.0*n-1.0)*psi1/x-psi0;
       chi = (2.0*n-1.0)*chi1/x-chi0;
       xi = complex(psi, -chi);
       an = (**(d+n-1)/refrel+n/x)*psi-psi1;
       an = an/((**(d+n-1)/refrel+n/x)*xi-xi1);
       bn = (refrel*(**(d+n-1))+n/x)*psi-psi1;
       bn = bn/((refrel*(**(d+n-1))+n/x)*xi-xi1);
       qsca = qsca+(2.0*n+1.0)*(abs(an)*abs(an)+abs(bn)*abs(bn));
       for (idum = 1; idum <= ndiv; idum++)
          {
          idum2 = 2*ndiv-idum;
          **(pi+idum-1) = **(pi1+idum-1);
```

```
        **(tau+idum-1)  =  n*(**(amu+idum-1))*(**(pi+idum-1))-
           (n+1.0)*(**(pi0+idum-1));
        **(s1+idum-1)  =  **(s1+idum-1)+fn*(an*(**(pi+idum-1))+
           bn*(**(tau+idum-1)));
        **(s2+idum-1)  =  **(s2+idum-1)+fn*(an*(**(tau+idum-1))+
           bn*(**(pi+idum-1)));
        if (idum != idum2)
           {
           p = 1;
           if (n%2 != 0) p = -1;
           it = -p;
           **(s1+idum2-1)  =  **(s1+idum2-1)+fn*(an*(**(pi+idum-1))*p+
              bn*(**(tau+idum-1))*it);
           **(s2+idum2-1)  =  **(s2+idum2-1)+fn*(an*(**(tau+idum-1))*it+
              bn*(**(pi+idum-1))*p);
           }
        }
     psi0 = psi1;
     psi1 = psi;
     chi0 = chi1;
     chi1 = chi;
     xi1  =  complex(psi1,-chi1);
     for (idum = 1; idum <= ndiv; idum++)
        {
        **(pi1+idum-1)  =  (2.0*n+1.0)/n*
           (**(amu+idum-1))*(**(pi+idum-1));
        **(pi1+idum-1)  =  **(pi1+idum-1)-(n+1)*
           (**(pi0+idum-1))/n;
        **(pi0+idum-1)  =  **(pi+idum-1);
        }
     }
  qsca  =  (2.0/(x*x))*qsca;
  dyndest(ndiv,  pi);
  dyndest(ndiv,  pi0);
  dyndest(ndiv,  pi1);
  dyndest(ndiv,  tau);
  dyndest(ndiv,  amu);
  return  (qsca);
  }
```

Input File

(1.0,0.0) (1.55, 0.0)

0.525 0.6328
11

Output File

ang	s11	s33	s34	pol
0	1	1	0	-0
9	0.78539	0.9994	0.034326	-0.004598
18	0.356897	0.986022	0.160184	-0.045854
27	0.076612	0.843603	0.394076	-0.364744
36	0.035536	0.686967	-0.491787	-0.534997
45	0.070184	0.959825	-0.280434	0.0096
54	0.057431	0.985371	0.163584	0.047793
63	0.021966	0.648043	0.621216	-0.440604
72	0.012596	0.203255	-0.516208	-0.831996
81	0.017375	0.795354	-0.605182	0.034167
90	0.01246	0.937497	0.260742	0.230462
99	0.006791	-0.007174	0.700647	-0.713472
108	0.009542	-0.039475	-0.653085	-0.756255
117	0.008634	0.536251	-0.795835	-0.281215
126	0.002274	0.967602	0.07958	-0.239612
135	0.00544	0.187531	-0.490882	-0.850804
144	0.016024	0.495254	-0.505781	-0.706334
153	0.018885	0.453277	-0.022682	-0.891081
162	0.019525	-0.391613	0.482752	-0.783319
171	0.030168	-0.962069	0.189556	-0.196194
180	0.038319	-1	2.18227e-20	8.729078e-20

Output Screen

qsca, qext, and qback = 3.105426 3.105426 2.925341

ang	s11	s33	s34	pol
0	1	1	0	-0
9	0.78539	0.9994	0.034326	-0.004598
18	0.356897	0.986022	0.160184	-0.045854
27	0.076612	0.843603	0.394076	-0.364744
36	0.035536	0.686967	-0.491787	-0.534997
45	0.070184	0.959825	-0.280434	0.0096
54	0.057431	0.985371	0.163584	0.047793
63	0.021966	0.648043	0.621216	-0.440604
72	0.012596	0.203255	-0.516208	-0.831996
81	0.017375	0.795354	-0.605182	0.034167
90	0.01246	0.937497	0.260742	0.230462
99	0.006791	-0.007174	0.700647	-0.713472
108	0.009542	-0.039475	-0.653085	-0.756255
117	0.008634	0.536251	-0.795835	-0.281215
126	0.002274	0.967602	0.07958	-0.239612

135	0.00544	0.187531	-0.490882	-0.850804
144	0.016024	0.495254	-0.505781	-0.706334
153	0.018885	0.453277	-0.022682	-0.891081
162	0.019525	-0.391613	0.482752	-0.783319
171	0.030168	-0.962069	0.189556	-0.196194
180	0.038319	-1	2.18227e-20	8.729078e-20

INITIAL DISTRIBUTION

Dr. Ralph Carabetta
Project Management
U.S. DOE/PETC
P.O. Box 10940
Pittsburgh, PA 15236-0940

Ms. Kay Downey
MS 58-M217
U.S. DOE/PETC
P.O. Box 10940
Pittsburgh, PA 15236-0940

Mr. James M. Ekmann
Director, Coal Combustion Division
U.S. DOE/PETC
P.O. Box 10940, MS 84-307
Pittsburgh, PA 15241

Dr. David Beecy, Director
Office of Advanced Research
Fossil Energy, FE-72
U.S. DOE/GTN
19901 Germantown Road
Germantown, MD 20585

Mr. Robert Wright
Office of Advanced Research
Fossil Energy, FE-72
U.S. DOE/GTN
19901 Germantown Road
Germantown, MD 20585

Mr. Philip M. Goldberg
Coal Utilization Division
U.S. DOE/PETC, 922-H
P.O. Box 10940
Pittsburgh, PA 15236-0940

Mr. James Hickerson
Coal Utilization Division
U.S. DOE/PETC, 922-H
P.O. Box 10940
Pittsbrugh, PA 15236-0940

Dr. Larry Ruth
Coal Utilization Division
U.S. DOE/PETC
P.O. Box 10940
Pittsburgh, PA 15236-0940

Mr. Cliff Smith
Coal Utilization Division
U.S. DOE/PETC, 922-H
P.O. Box 10940
Pittsbrugh, PA 15236-0940

Mr. James Jovanovich
PM-01, MS922-206
U.S. DOE/PETC, 922-H
P.O. Box 10940
Pittsburgh, PA 15236-0940

Mr. Laurance L. Oden
Albany Research Facility, Bureau of Mines
U.S. Department of the Interior
Albany, OR 97321

Professor János Beér
Massachusetts Institute of Tech.
Department of Chemical Engineering
66-552
Cambridge, MA 02139

Professor Robert Essenhigh
Mechanical Engineering Department
Ohio State University
206 West 18th Avenue
Columbus, OH 43210

Professor Thomas H. Fletcher
Chemical Engineering Department
Brigham Young University
350 CB
Provo, UT 84602

Professor Robert Hurt
Division of Engineering, Box D
Brown University
Providence, RI 02912

Professor Bryan M. Jenkins
University of California, Davis
Biological and Ag. Eng. Dpt.
Davis, CA 95616-5294

Dr. Michael L. Jones
Energy and Mineral Research Center
University of North Dakota
Box 8213, University Station
Grand Forks, ND 58202
Attn: Dr. Steve Benson

Professor John P. Longwell
Chemical Engineering Department
Massachusetts Institute of Technology
Room 66554
Cambridge, MA 02139

Professor Reginald E. Mitchell
High Temperature Gasdynamics Lab
Stanford University
Mechanical Engineering Department
Palo Alto, CA 94305

Professor Ronald Pugmire
Vice President for Research
University of Utah
210 Park Building
Salt Lake City, UT 84112

Professor Daniel E. Rosner
Director, High Temperature Chem Engr Lab
Yale University
P.O. Box 2159
New Haven, CT 06520-8167

Professor Adel Sarofim
Department of Chemical Engineering
Massachusetts Institute of Technology
66-466
Cambridge, MA 02139

Professor Philip Smith
Department of Chemical Engineering
University of Utah
2250 Merrill Engineering Bldg
Salt Lake City, UT 84112

Professor Terry Wall
Department of Chemical & Materials Engr.
The University of Newcastle
Newcastle, NSW 2308
Australia

Professor Jost Wendt
Department of Chemical Engineering
University of Arizona
Tuscon, AZ 85721

Dr. Seymour B. Alpert
P.O. Box 10412
Electric Power Research Institute
3412 Hillview Avenue
Palo Alto, CA 94308

Dr. Richard Bain, Manager
Biomass Power Program
National Renewable Energy Laboratory
1617 Cole Boulevard
Golden, CO 80401-3393

Mr. Richard W. Borio
Combustion Engineering Inc.
1000 Prospect Hill Road, P.O. Box 500
Windsor, CT 06095
Attn: Mr. Michael Hargrove

Chester M. Bowling
Manager Tech. Support & Mrktng
ARCO Coal Company
555 Seventeenth St.
Denver, CO 80202

Mr. Richard W. DeSollar
Fuels Coordinator
Central Illinois Public Service Co.
607 East Adams Street
Springfield, Il 62701

Mr. Larry Dora
Engineering Supervisor
Northern Indiana Public Service Co.
P.O. Box M-720
Gary, IN 46401

Dr. Woodrow Fiveland, Supervisor
Heat Transfer & Fluid Mechanics Section
Babcock & Wilcox
1562 Beeson St.
Alliance, OH 44601

Dr. J. Peter Gorog
Research and Development
Pulp, Paper and Packaging
Weyerhaeuser Company
WTC 2H22
Tacoma, WA 98477

Mr. Peter Torslev Jensen
ELSAM
Fuel Department
DK-7000 Fredericia
Denmark

Dr. Flynt Kennedy, Vice President
Research & Development
Consolidation Coal Co.
4000 Brownsville Road
Library, PA 15129
Attn: Dr. Anthony Fonseca

Dr. John Lytle
Mineral Engineering Laboratory
Illinois State Geological Survey
Oak and Gregory Sts.
Champaign, IL 61820

Dr. John S. Maulbetsch
Exploratory Research
EPRI
3412 Hillview Avenue
Palo Alto, CA 94303

Dr. Arun K. Mehta
P.O. Box 10412
Electric Power Research Institute
3412 Hillview Avenue
Palo Alto, CA 94308

Mr. Thomas R. Miles
Consulting Design Engineer
5475 SW Arrowwood Lane
Portland, OR 97225

Dr. Thomas Milne
National Renewable Energy Laboratory
1617 Cole Boulevard
Golden, CO 80401-3393

Dr. Ralph P. Overend
National Renewable Energy Lab
1617 Cole Boulevard
Golden, CO 80401-3393

Mr. Eric H. Reichl
P.O. Box 472
Princeton, NJ 08542

Dr. Dan Seery
United Technologies Research Center
Combustion Sciences
Silver Lane, MS 30
East Hartford, CT 06108

Mr. Ian W. Smith, Manager
Coal Utilization Program
CSIRO
51 Delhi Road, P.O. Box 136
North Ryde, NSW, 2113
Australia

Professor L. Douglas Smoot
Consulting Design Engineer
5475 SW Arrowwood Lane
Portland, OR 97225

Mr. Jerry Sullivan
Project Director
PSI Energy
1000 East Main Street
Plainfield, IN 46168

Dr. David A. Tillman
Foster Wheeler Environmental Corporation
2525 Natomas Park Drive, Suite 250
Sacramento, CA 95833-2900

Mr. Stanley Vecci, Director
Energy Systems Lab/Research Dev Div
Babcock & Wilcox
1562 Beeson Street
Alliance, OH 44601
Attn: Mr. John Berthold
Mr. Thomas Morris
Mr. Larry Rodgers
Dr. Hamid Sarv
Mr. James Warchol
Mr. Ralph Bailey
Mr. George Farthing

Mr. Ben Ziesmer
Fuel Coordinator
Northern Indiana Public Services Co.
5265 Hohman Ave.
Hammond, IN 46320

MS0701 R.W. Lynch, 6100

MS0735 D.E. Arvizu, 6200
Attn: 6211 G.A. Carlson
6212 H.R. Stephens
6203 A.P. Sylwester

MS0704 P.C. Klimas, 6201
Attn: 6215 J. Chavez
6215 K.S. Rawlinson

MS9001 J.C. Crawford, 8000
Attn: 8100 M.E. John
8113 J.C. Swearengen
8700 R.C. Wayne
8713 J.F.C. Wang
8713 D.K. Ottesen
8714 M. Perra

MS9054 W.J. McLean, 8300
Attn:

8302	W. Bauer	8351	L.A. Rahn
8304	K. Wilson	8353	F.P. Tully
8341	W. Wolfer	8355	G.A. Fisk
8342	R. Stulen	8362	R.W. Carling
8347	A. Pontau	8366	C.M. Hartwig

Org.	Bldg.	Name	Rec'd by	Org.	Bldg.	Name	Rec'd by

Sandia National Laboratories